Supplementary Materials for

Mechanism of homodimeric cytokine receptor activation and dysregulation by oncogenic mutations

Stephan Wilmes, Maximillian Hafer, Joni Vuorio, Julie A. Tucker, Hauke Winkelmann, Sara Löchte, Tess A. Stanly, Katiuska D. Pulgar Prieto, Chetan Poojari, Vivek Sharma, Christian P. Richter, Rainer Kurre, Stevan R. Hubbard, K. Christopher Garcia, Ignacio Moraga, Ilpo Vattulainen*, Ian S. Hitchcock*, Jacob Piehler*

*Corresponding author. Email: ilpo.vattulainen@helsinki.fi (I.V.); ian.hitchcock@york.ac.uk (I.S.H.); piehler@uos.de (J.P.)

Published 7 February 2020, *Science* **367**, 643 (2020)
DOI: 10.1126/science.aaw3242

This PDF file includes:

Other supplementary material for this manuscript includes:

Materials and Methods

Plasmids

For single-molecule fluorescence microscopy, a non-fluorescent (Y66F) variant of monomeric green fluorescent protein (mXFP) was N-terminally fused to human TpoR, human EpoR and rabbit GHR, respectively. These constructs as well as indicated truncations or mutations were inserted into a modified version of pSems-26m (Covalys) which includes the N-terminal signal sequence of Igκ followed by a hemagglutinin (HA)-tag upstream of the mXFP tag (pSems-leader). E3-tagged or E3-tag-mXFP-tagged receptors were cloned accordingly using the 21 amino acid E3-tag as described previously (*23*). For negative control experiments, a model transmembrane protein, comprised of an N-terminal monomeric enhanced green fluorescent protein (mEGFP) tag linked to an artificial transmembrane domain $(ALA)_7KSSR$ was inserted into the same vector. For positive control experiments maltose binding protein (MBP) was inserted between mEGFP and the artificial transmembrane domain for dimerization via a monoclonal antibody against MBP. The effective degree of cell surface labeling achieved by dye-conjugated nanobodies was determined using either HaloTag-mEGFP-IFNAR2 or SNAPf-mEGFP-IFNAR1. For cellular micropatterning, the receptor genes N-terminally fused to HaloTag and mTagBFP were inserted into pSems-leader (HaloTag-mTagBFP-TpoR, HaloTag-mTagBFP-EpoR and HaloTag-mTagBFP-GHR, respectively). As negative controls, TpoR truncated after R514 (TpoR-514Δ) as well as TpoR with mutations in the box 1 and 2 motifs (TpoR Box1+2: W529A, S531A, P533A, D534A, E569A, I570A and L571A) to abolish JAK binding were cloned accordingly. For the comparison of mXFP-tagged and untagged receptors, EpoR, TpoR and rGHR including their original N-terminal signal sequences as well as a C-terminal 2A self-cleaving peptide (P2A) (*53*) followed by mTagBFP including a nuclear localization (NLS) sequence were cloned into the pSems-26m backbone. Truncations of the extracellular domains of TpoR (upstream of Y483) and EpoR (upstream of P245) were created by PCR according to standard protocols.

All mutants or truncations of JAK2 or TYK2 were C-terminally fused to mEGFP and inserted into pSems-26m. JAK2 was truncated after I827 (JAK2 ΔTK) or E543 (JAK2 ΔPK-TK) to remove the JH1 (tyrosine kinase, TK) domain or both JH1 and JH2 (pseudokinase, PK) domains, respectively. TYK2 was similarly truncated after Y896 (TYK2 ΔTK) or I588 (TYK2 ΔPK-TK). Point mutations within the receptor and the kinases were generated by PCR according to standard protocols (and see below).

For activity assays by western blot and phospho-flow cytometry, untagged JAK2 wt and mutants were cloned into pIRES2-EGFP (Clontech). Point mutants of JAK2 and TYK2 were generated by site-directed polymerase chain reaction (PCR) mutagenesis using either CloneAmp™ HiFi PCR Premix (TaKaRa/Clontech) or Phusion HotStart Flex 2X Master Mix (NEB/ThermoFisher) and overlapping primers. Reactions were set up in a final volume of 10 µL containing 4 ng template plasmid DNA, and a final concentration of 60 nM of each primer. When using Phusion HotStart Flex 2X Master mix, DMSO was included at a final concentration of 3% (v/v). For CloneAmp™ HiFi polymerase, the following reaction conditions were used: 98ºC for 30 s, then 18 cycles of 98ºC for 10 s, 55ºC for 30 s then 72ºC for 150 or 300 s, and finally 72ºC for 600 s. For Phusion HotStart Flex polymerase, the following reaction conditions were used: 98ºC for 60 s, then 25 cycles of 98ºC for 15 s then 72ºC for 330 s, and finally 72ºC for 600 s. Template DNA was removed by digestion with *Dpn*I (NEB, 0.2 U, 90 min at 37ºC followed by heat inactivation for 20 min at 80ºC), and 1 µL PCR reaction was then used to transform 25 µL chemically competent *E. coli* DH5α (Invitrogen/ThermoFisher). Plasmids were isolated from overnight cultures of single colonies using a QIAprep spin miniprep kit (QIAGEN), and

mutations confirmed by Sanger sequencing (Eurofins Genomics) across the entire JAK2/TYK2 open reading frame (ORF). Multiple mutants were generated by using an appropriate, sequence-verified single or double mutant as template for a second or third round of PCR mutagenesis. For use in transfection experiments, sequence-verified plasmids were amplified using a GenElute™ HP Plasmid MidiPrep Kit (Sigma Aldrich) according to the manufacturer's instructions. DNA concentrations were determined using a NanoDrop 2000 (ThermoScientific), and integrity of plasmid DNA verified by agarose gel electrophoresis.

The features and applications of different receptor and JAK constructs are summarized here:

Denomination	**Construct (residues)**	**Description and application**
mXFP-TpoR	pSems-leader-HA-mXFP-TpoR (25-635)	mXFP-tagged TpoR for single molecule microscopy
mXFP-ΔECD-TpoR	pSems-leader-HA-mXFP-TpoR (482-635)	mXFP-tagged TpoR lacking the extracellular domain for single molecule microscopy
mXFP-EpoR	pSems-leader-HA-mXFP-EpoR (25-508)	mXFP-tagged EpoR for single molecule microscopy
mXFP-EpoR-ΔECD	pSems-leader-HA-mXFP-EpoR(244-508)	mXFP-tagged EpoR lacking the extracellular domain for single molecule microscopy
mXFP-rGHR	pSems-leader-HA-mXFP-rGHR (19-638)	mXFP-tagged rabbit GHR for single molecule microscopy
TpoR	pSems-TpoR (1-635)-P2A-NLS-BFP	Untagged TpoR as control for activity analysis by phospho-flow cytometry
EpoR	pSems-EpoR (1-508)-P2A-NLS-BFP	Untagged EpoR as control for activity analysis by phospho-flow cytometry
E3-TpoR	pSems-leader-HA-E3-tag-TpoR(25-635)	E3-tagged TpoR for single molecule microscopy
E3-EpoR	pSems-leader-HA-E3-tag-EpoR (25-508)	E3-tagged EpoR for single molecule microscopy
E3-mEGFP-EpoR	pSems-leader-HA-E3-tag-mEGFP- EpoR (25-508)	E3- and mEGFP-tagged EpoR for single molecule microscopy
mEGFP-TMD	pSems leader-HA-mEGFP-(ALA)7KSSR	Negative control for single molecule microscopy
mEGFP-MBP-TMD	pSems leader-HA-mEGFP-MBP-(ALA)7KSSR	Positive control for single molecule microscopy
HaloTag-mEGFP-IFNAR2	pSems-leader-HA-HaloTag-mEGFP IFNAR2(27-515)	IFNAR1 with N-terminal HaloTag and mEGFP for quantifying the DOL at single molecule level
SNAPf-mEGFP-IFNAR1	pSems-leader-HA-HaloTag-mEGFP IFNAR1(28-557)	IFNAR1 with N-terminal SNAPf and mEGFP for quantifying the DOL at single molecule level

Denomination	Construct	Description
HaloTag-mTagBFP-TpoR	pSems-leader-HA-HaloTag-mTagBFP-TpoR(25-635)	TpoR with N-terminal HaloTag and mTagBFP as bait for cell micropatterning
HaloTag-mTagBFP-TpoR-514Δ	pSems-leader-HA-HaloTag-mTagBFP-TpoR(25-514)	TpoR lacking the entire intracellular domain with N-terminal HaloTag and mTagBFP as bait for cell micropatterning
HaloTag-mTagBFP-EpoR	pSems-leader-HA-HaloTag-mTagBFP-EpoR(25-508)	EpoR with N-terminal HaloTag and mTagBFP as bait for cell micropatterning
HaloTag-mTagBFP-rGHR	pSems-leader-HA-HaloTag-mTagBFP-rGHR(19-638)	GHR with N-terminal HaloTag and mTagBFP as bait for cell micropatterning
mXFP-IFNGR2	pSems leader HA mEGFP-Y66F IFNGR2(28-337)	mXFP-tagged IFNGR2 for single molecule microscopy
JAK2-mEGFP	pSems-JAK2 (1-1132)-mEGFP	Full-length JAK2 with C-terminal mEGFP for single molecule microscopy
JAK2	pIRES2-EGFP JAK2 (1-1132)	Full-length JAK2 for activity assays by western blot
JAK2-ΔTK-mEGFP	pSems JAK2 (1-827)-mEGFP	JAK2 lacking the TK domain for single molecule microscopy
JAK2-ΔPKTK-mEGFP	pSems-JAK2-(1-543)-mEGFP	JAK2 lacking TK and PK domains for single molecule microscopy and cell micropatterning
TYK2-mEGFP	pSems-TYK2 (1-1187)-mEGFP	Full length TYK2 with C-terminal mEGFP for single molecule microscopy
TYK2-ΔTK-mEGFP	pSems-TYK2 (1-896)-mEGFP	Tyk2 lacking the TK domain for single molecule microscopy
TYK2-ΔPKTK-mEGFP	pSems-TYK2 (1-588)-mEGFP	TYK2 lacking TK and PK domains for single molecule microscopy and cell micropatterning

Protein expression and purification

For cell surface labeling, the anti-GFP nanobody (NB) "enhancer" was used, which binds mEGFP with a 0.3 nM binding affinity (*54*). NB was cloned into pET-21a with an additional cysteine at the C-terminus for site-specific fluorophore conjugation in a 1:1 fluorophore:nanobody stoichiometry. Furthermore, a $(PAS)_5$ sequence to increase protein stability and a His-tag for purification were fused at the C-terminus. Protein expression in *E. coli* Rosetta (DE3) and purification by immobilized metal ion affinity chromatography was carried out by standard protocols. Purified protein was dialyzed against HEPES pH 7.5 and reacted with a two-fold molar excess of DyLight 800 (ThermoFisher, DY800) maleimide (ThermoFisher), DY-647P1 (DY647) maleimide (Dyomics), ATTO 643 (AT643) maleimide and ATTO Rho11 (Rho11) maleimide (ATTO-TEC GmbH), respectively. After 1 h, a 3-fold molar excess (with respect to the maleimide) of cysteine was added to quench excess dye. Protein aggregates and free dye were subsequently removed by size exclusion chromatography (SEC). A labeling degree of 0.9-1:1 fluorophore:protein was achieved as determined by UV/Vis spectrophotometry. The NB-based dimerizer was obtained by reacting purified NB with 1,11-bismaleimido-triethyleneglycol (ThermoFisher #22337) in a 2:1 ratio in HEPES pH 7.5 followed by SEC.

Recombinant Epo, GH and ECD-GHR were produced in Hi5 insect cells using baculoviral infection according to standard protocols. Recombinant human Tpo was a gift from Don Foster (Zymogenetics, Seattle, WA). For fluorescence labeling, 56 µM Tpo was incubated with 53 µM Alexa Fluor 647 (AF647) NHS ester (Invitrogen; stock solution at 2 mg/mL in dimethyl sulphoxide (DMSO, Sigma)) in a final volume of 150 µL 0.53 X phosphate buffered saline (PBS; Sigma) supplemented with 27 mM $NaHCO_3$ (Fluka) for 1 h at 22 ºC with shaking. Unreacted dye was removed by applying the reaction mixture to a 0.5 mL 7 kDa molecular weight cutoff (MWCO) Zeba™ spin desalting column (Invitrogen), and the dye: protein ratio determined spectrophotometrically. This yielded AF647-Tpo with an average dye: protein ratio ~ 0.7. In a second step, in order to increase the dye:protein ratio, 27 µM AF647-Tpo was incubated with 53 µM AF647 NHS ester under the reaction conditions described above. Unreacted dye was removed as described above, except that the spin column was pre-equilibrated with 1 X PBS before use. This yielded AF647-Tpo with a dye:protein ratio ~2:1, and this was used for subsequent experiments. The integrity and homogeneity of the labelled Tpo were confirmed by sodium dodecyl sulfate (SDS)–polyacrylamide gel electrophoresis (PAGE) and SEC-multi-angle laser light scattering (MALS). Bovine GH was purchased from Prospecbio. YbbR-tagged human GH wt and G146R were expressed in *E. coli* and refolded from inclusion bodies by standard protocols. After purification by anion exchange and size exclusion chromatography, proteins were enzymatically labeled using DY647 and DY547 maleimide (Dyomics) conjugated to Coenzyme A as described previously (*55*). Labeling degree was determined by UV/Vis spectrophotometry.

A K4 peptide including a C-terminal Cys residue was custom synthesized by Genscript Biotech Co. Rho11-maleimide (ATTO-TEC GmbH) and DY647 maleimide, respectively were coupled under aqueous conditions at pH 6.8. The conjugates ^{Rho11}K4 and ^{DY647}K4 were purified by reversed phase HPLC and their identity was confirmed by MALDI.

Western blot, phospho-flow cytometry staining and antibodies

HeLa clones were serum starved for 16 hours prior to cytokine stimulation for 10 minutes. Cells were then lysed in Nonidet P40 (NP-40) lysis buffer (50 mM tris(hydroxymethyl)aminomethane (Tris)-HCl, pH 7.4, 1% NP-40, 150 mM NaCl, 1 mM ethylenediaminetetraacetic acid (EDTA), 10 mM β-glycerolphosphate, 1 mM Na_3VO_4, 10 mM NaF) containing 1% protease inhibitors (Sigma-Aldrich #P8340). Denatured proteins were fractionated by SDS-PAGE and transferred to polyvinylidene difluoride (PVDF) membranes. Protein expression was detected by incubating with anti-phospho JAK2 (Y1007/8; #3771), anti-JAK2 (#3230), anti-phospho STAT5 (Y694; #9359), anti-STAT5 (#9363), anti-HA (#3724) followed by anti-rabbit-HRP (#7074) or anti-β actin-HRP (#5125) (all Cell Signaling Technologies) and visualized by chemiluminescent detection reagent (ECL-prime; GE Healthcare #29018903). The phosphorylated JAK2 (pJAK2) was quantified using ImageJ/Fiji (*53*). Each lane from the blot was selected by drawing a box with similar dimensions and the intensity measured using the *'Analyze/ Gel/ GelAnalyzerOptions'* in Fiji. pJAK2: JAK2 intensity ratios were obtained and normalized to the corresponding JAK2 wt sample and then plotted using GraphPad Prism v8.0.

For quantifying STAT3 and STAT5 by flow cytometry (Cytoflex S, Beckman Coulter), HeLa, HEK293 and HeLa clones stably expressing mXFP-tagged receptors were first detached using PBS + EDTA (2 mM). Detached cells could be used for several assays (see below). Cells were immunostained after fixation (2% paraformaldehyde) and permeabilization in ice-cold methanol (100% v/v). Anti-pSTAT5 (Cell Signaling Technologies, #9365) or anti-pSTAT3 (Biolegend, #651007) antibodies conjugated to Alexa Fluor 647 were used at a 1:100 dilution.

Mean fluorescence intensity (MFI) values were plotted together with standard error of the mean (SEM). The following experimental conditions were used in different types of experiments:

- Dose-response curves: Cells were stimulated with indicated concentrations of ligand for 15 min at 37°C.
- Cytokine stimulation and inhibitor treatment: Cells were transfected with the indicated receptor and/or JAK2 constructs using the polyethyleneimine (PEI, Polysciences Inc, # 233966) method according to standard protocols. As a negative control, cells were treated with the JAK inhibitor Tofacitinib (3 μM for 30 min at 37°C) before cytokine stimulation (15 min at 37°C).
- Receptor density-dependent basal pSTAT activity: PEI-transfected cells expressing mXFP-tagged receptors were cell surface stained with ^{DY800}NB (10 nM) for 20 min on ice. JAK2 expression was detected using the EGFP signal. Cell surface receptor densities were quantified via DY800 fluorescence. The fluorescence intensity was translated into absolute receptor densities by calibrating the ^{DY800}NB signal using a stable cell line with known cell surface density determined by single molecule imaging (2.5 receptors/μm^2).

Quantification of TpoR cell surface expression by flow cytometry

Ba/F3-parental, Ba/F3-MPL, HeLa, HeLa-MPL, UT7 and UT7-Tpo cells were plated at 1x10^5 cells per well in a total volume of 25 μL, and treated with increasing concentrations of AF647-Tpo (dye:protein 2.0) for 1 hr at RT whilst shaking at 600 rpm. Cells were washed three times in FACS buffer (0.5% w/v BSA, 0.05% v/v sodium azide in PBS) and analysed by flow cytometry on a Cytoflex LX. In these experiments, a concentration of 50 μg/mL (~680 nM) AF647-Tpo was shown to be saturating. The mean fluorescence intensity (MFI) values at saturating AF647-Tpo for cell lines expressing MPL were corrected by background subtraction using the values for the corresponding parental (non-MPL expressing) cell line at the same AF647-Tpo concentration.

Cell culture for microscopy

HeLa cells were cultivated at 37°C and 5% CO_2 in MEM's Earle's medium with stable glutamine supplemented with 10% fetal bovine serum (FBS), non-essential amino acids and HEPES buffer without addition of antibiotics. For microscopy experiments, confluent cells were trypsinated and transferred to a 60 mm cell culture dish (1:10 dilution) and transiently transfected via calcium-phosphate-precipitation according to standard protocols (*56*). Transfected cells were transferred onto 25 mm glass coverslips (1:20 dilution) coated with a poly-L-lysine-graft-(polyethylene glycol) copolymer functionalized with RGD to minimize non-specific binding of fluorescent NBs (*57*). Single-molecule imaging experiments were conducted 48 h post transfection after mounting the coverslips into custom-designed microscopy chambers with a volume of 1 mL. For experiments with GHR, cells were kept in serum-reduced (2% FBS) media overnight, supplemented with 300 nM of the soluble ECD of human GHR in order to scavenge bovine GH. 4 hours before imaging, cells were washed 4x with PBS, and coverslips were transferred to clean 3 cm dishes containing serum-free media. For cellular micropatterning, 24-36 hours after transfection cells were plated on chemically modified cover glasses for 15-20 hours with medium containing penicillin and streptomycin (PAA Laboratories).

Single-molecule fluorescence imaging

Single-molecule imaging experiments were conducted by total internal reflection fluorescence (TIRF) microscopy with an inverted microscope (Olympus IX71) equipped with a triple-line total internal reflection (TIR) illumination condenser (Olympus) and a back-

illuminated electron multiplied (EM) CCD camera (iXon DU897D, Andor Technology) as described in more detail previously (*19, 58*). A 150 × magnification objective with a numerical aperture of 1.45 (UAPO 150 × /1.45 TIRFM, Olympus) was used for TIR illumination of the sample. All experiments were carried out at room temperature in medium without phenol red, supplemented with an oxygen scavenger and a redox-active photoprotectant to minimize photobleaching (*59*). For cell surface labeling of mXFP-tagged receptors, DY647- (or AT643-) and Rho11-labeled NBs were added to the medium at equal concentrations (2 nM each) that ensured > 90% binding given the 0.3 nM binding affinity. After incubation for at least 5 min, image acquisition was started with the labeled NBs kept in the bulk solution during the whole experiment in order to ensure high equilibrium binding. Negative and positive control proteins for co-localization were labeled under the same conditions. Under these conditions, an effective labeling efficiency of ~70% is achieved for mXFP-tagged cell surface proteins as determined by single-molecule co-locomotion analysis of model proteins fused to either mEGFP and SNAPf or HaloTag (SNAPf-mEGFP-IFNAR1 & HaloTag-mEGFP-IFNAR2) as previously described (*58*). E3-tagged receptors were labeled by incubating with 10 nM ^{Rho11}K4 or ^{DY647}K4 for 10 min at room temperature. After washing with 3 mL medium, imaging experiments were immediately started. HaloTag-fusion proteins were labeled with 50 nM HaloTag-Ligand Tetramethylrhodamine (HTL-TMR, Promega) and SNAPf-tagged proteins were labeled with 80 nM SNAP-Surface DY647 (New England Biolabs, Inc.) at 37°C for 15 min and washed 5 times with pre-warmed PBS to remove unreacted dyes. Dimerization of cytokine receptors was probed before and after incubation with 5 nM of the corresponding ligand. Dimerization of the positive control mEGFP-MBP-TMD was induced using 20 nM monoclonal antibody against MBP (Santa Cruz Biotechnology, Inc.sc-13564). Pharmacological inhibition of JAK activity was achieved using the JAK inhibitor Ruxolitinib (Adooq Bioscience). Ruxolitinib was added to the culture medium at 3 μM 4h prior to imaging experiments.

For single molecule co-localization and co-tracking experiments, orange (Rho11 and TMR) and red (DY647 and AT643) emitting fluorophores were simultaneously excited by illumination with a 561 nm laser (CrystaLaser) at 0.95 mW (~32 W/cm^2) and a 642 nm laser (Omicron) at 0.65 mW (~22 W/cm^2). Fluorescence was detected using a spectral image splitter (DualView, Optical Insight) with a 640 DCXR dichroic beam splitter (Chroma) combined with the bandpass filter 585/40 (Semrock) for detection of Rho11/TMR and 690/70 (Chroma) for detection of DY647/AT643 dividing each emission channel into 512 x 256 pixels. Image stacks of 150 frames were recorded for each cell at a time resolution of 32 ms/frame. For PAINT experiments, 10 nM of a low-affinity GFP binder labeled with AT643 was added to the medium. To obtain long-timescale receptor distribution at the cell surface, 16000 frames were recorded over 8.5 min. Single molecule FRET (smFRET) was probed by alternating laser excitation (ALEX). To this end, mXFP-tagged receptors were labeled with Rho11 and AT643 as described above. Two-color image acquisition was performed with alternating excitation at 561 nm and at 642 nm frame-by-frame at a frame rate of 50 Hz using a fast (EM) CDD camera (iXon Ultra 897, Andor Technology). Thus, a total time resolution of 25 frames/s was achieved, which was sufficient for reliable tracking.

Single-molecule analyses

Single-molecule localization was carried out using the multiple-target tracing (MTT) algorithm (*60*) and tracking was performed using the u-track algorithm (*61*). Single molecule PAINT images were reconstructed from emitters localized within 16000 frames. Diffusion constants were determined by mean square displacement analysis within a time window of 320 ms (10 frames). For co-tracking analysis, immobile molecules were identified by

spatiotemporal cluster analysis (*62*) and removed from the dataset (typically ~15-20% of all localizations) prior to quantifying diffusion and dimerization because this fraction is biased by (i) labeled NBs non-specifically adsorbed onto the coverslip surface and (ii) endosomes located close to the plasma membrane. Receptor dimerization was quantified based on sequential co-localization and co-tracking analysis as described in detail recently (*58*): after aligning Rho11 and DY647 channels with sub-pixel precision by using a spatial transformation based on a calibration measurement with multicolor fluorescent beads (TetraSpeck microspheres 0.1 µm, Invitrogen), individual molecules detected in both spectral channels of the same frame within a distance threshold of 100 nm were considered co-localized. For single-molecule co-tracking analysis, the MTT algorithm was applied to this dataset of co-localized molecules to reconstruct co-locomotion trajectories (co-trajectories) from the identified population of co-localizations. For the co-tracking analysis, only co-trajectories with a minimum of 10 consecutive steps (320 ms) were considered. This cut-off was determined based on systematic analysis of a negative control experiment with non-interacting model transmembrane proteins (*58*) in order to minimize background from random co-localization (Fig. S5A). The relative fraction of co-tracked molecules was determined with respect to the absolute number of trajectories from both channels and corrected for dimers stochastically double-labeled with the same fluorophore species as follows:

$$AB^* = \frac{AB}{2\times\left[\left(\frac{A}{A+B}\right)\times\left(\frac{B}{A+B}\right)\right]} \qquad \textit{Eqn. 1}$$

$$rel.\ co-locomotion = \frac{2\times AB^*}{(A+B)} \qquad \textit{Eqn. 2}$$

where A, B, AB and AB* are the numbers of trajectories observed for Rho11, DY647, co-trajectories and corrected co-trajectories, respectively. Box plots were used for visualization and indicate the data distribution of 2nd and 3rd quartile (box), median (line), mean (square) and 1.5× interquartile range (whiskers). Each data point represents the analysis from one cell with a minimum of 10 cells measured for each condition. Statistical significances were calculated by unpaired t-tests.

For heterodimerization experiments of mXFP-TpoR and SNAPf-EpoR, the relative fraction of dimerized receptors was calculated from the number of co-trajectories relative to the number of TpoR trajectories as EpoR was expressed in moderate excess (~2 fold).

Particle image cross correlation spectroscopy (PICCS) was applied for co-tracking-independent quantification of co-localized molecules (*63*). PICCS analysis was performed as described previously (*24*) to determine the correlated fraction α of particles in channel A which are co-localized with particles in channel B:

$$C_{cum}(r) = \alpha P_{cum}(r) + c_{channelB} \cdot \pi r^2 \qquad \textit{Eqn. 3}$$

For randomly distributed particles without a correlated fraction α, the function is linear at increasing search area r^2 with the slope given by the density of particles in channel B. The offset of this linear term corresponds to the correlated fraction α.

For quantifying receptor dimerization by smFRET, molecules were localized in the sensitized acceptor fluorescence channel. False-positive smFRET signals were removed by co-localization with directly excited acceptor signals. For this purpose, the FRET and acceptor channels were co-localized with a threshold of 200 nm to compensate for temporal shift due to alternating excitation. Based on the co-localization data the relative dimerization was determined and corrected for dimers stochastically double-labeled with the same fluorophore as described for co-tracking experiments above.

Calculation of equilibrium constants and free energy contributions ΔΔG

The two-dimensional equilibrium dissociation constants (K_D^{2D}) were calculated according to the law of mass action for a monomer-dimer equilibrium:

$$K_D^{2D} = \frac{[M]^2}{[D]} = \frac{([M]_0 - 2[D])^2}{[D]} \qquad \textit{Eqn. 4}$$

Where $[M]$ and $[D]$ are the concentrations of the monomer and the dimer, respectively, and $[M]_0$ is the total receptor concentration. The relative dimerization levels D_{rel} were plotted as a function of K_D^{2D} according to the physically relevant solution of the square equation:

$$D_{rel} = \frac{2[D]}{[M]_0} = \frac{2}{[M]_0}\left[\frac{\left([M]_0 + \frac{K_D^{2D}}{4}\right)}{2}\right] - \sqrt{\frac{\left([M]_0 + \frac{K_D^{2D}}{4}\right)^2}{4} - \frac{[M]_0^2}{4}} \qquad \textit{Eqn. 5}$$

assuming an average $[M]_0$ of 2 molecules/μm². Measured relative dimerization levels from co-tracking experiments were normalized to the relative dimerization level of the positive control (0.26) prior to calculating the corresponding K_D^{2D}:

$$K_D^{2D} = \frac{2(1 - 2D_{rel} + D_{rel}^2)[M]_0}{D_{rel}} \qquad \textit{Eqn. 6}$$

Free energy contributions were calculated from the changes in K_D^{2D} according to:

$$\Delta\Delta G = -RT \times ln\left(\frac{K_2}{K_1}\right) \qquad \textit{Eqn. 7}$$

with the universal gas constant R and the absolute temperature T.

The relative dimerization levels D_{rel} from smFRET experiments were calculated from the number of molecules detected in the sensitized fluorescence channel and the total number of molecules detected by direct acceptor excitation. For each sampled cell, the 2D dissociation constant (K_D^{2D}) was determined using the law of mass action (Eqn. 6) given the observed total receptor density and relative dimerization level taking the effective DOL of 70% into account. From the pooled experiments an average dissociation constant as well as its standard error could be estimated. The final dose response curves were then generated by plugging the respective average dissociation constant and its 95% confidence bounds into Eqn. 5.

Cell micropatterning and image analysis

Micropatterned functionalized surfaces for live cell micropatterning were fabricated by microcontact printing as described previously (*64*). Poly(dimethylsiloxane) (PDMS) stamps were generated from basic elastomer (Sylgard 184, Dow Chemicals) mixed with curing agent (Dow Chemicals) in a 10:1 ratio, and applied to a silicon master at 80°C overnight. The silicon master containing an array of lines with a width of 5 μm, a spacing of 10 μm and a depth of 3 μm was generated by photolithography using a custom designed beam mask (nb technologies GmbH). Standard glass coverslips for fluorescence microscopy were cleaned in a plasma cleaner for 10 minutes, followed by inking of the stamp with 0.5 mg/mL poly-L-lysine-graft-poly (ethylene glycol) (PLL-PEG) conjugated with the HaloTag ligand (PLL-PEG-HTL) (*65*) in PBS buffer for 10 minutes. For PLL-PEG-HTL transfer, stamps were placed onto the glass coverslips for 10 minutes to generate HTL patterns. After removing the stamps, the coverslips were incubated with a mixture of 0.002 mg/mL PLL-PEG conjugated with the peptide RGD (PLL-PEG-RGD) (*64*) and 0.1 mg/mL of methoxy-terminated PLL-PEG (PLL-PEG-MeO) in PBS buffer for 1 min to backfill the uncoated area to allow cell adhesion. The surface was then rinsed in MilliQ water and dried with nitrogen.

For micropatterning experiments, TIRF microscopy was performed using an inverted microscope (Olympus IX81) equipped with a 4-line TIRF condenser (Olympus TIRF 4-Line LCl), a CMOS camera (ORCAFlash 4.0, 2048×2048 pixel from Hamamatsu) and lasers at 405 nm (100 mW), 488 nm (150 mW), 561 nm (150 mW) and 640 nm (140 mW). A 60× objective with a numerical aperture of 1.49 (UAPON 60×/1.49, Olympus) or a 100× objective with a numerical aperture of 1.49 (UAPON 100×/1.49, Olympus) was used for TIRF excitation. The excitation beam was reflected into the objective by a quad-band dichroic mirror (zt405/488/561/640rpc) and the fluorescence was detected through a quadbandpass filter (BrightLine HC 446/523/500/677). For multicolor experiments, a fast emission filter wheel equipped with suitable emission filters (BrightLine HC 445/45, BrightLine HC 525/50, BrightLine HC 600/37 and BrightLine HC 697/58) was utilized to avoid spectral cross-talk. Data acquisition was performed with the acquisition software Olympus CellSens 2.2. Image analysis and image processing were performed using ImageJ/ Fiji (NIH, Bethesda, MD). Image processing comprised cropping, scaling, rotation as well as adjustment of brightness and contrast levels. Stabilities of JAK-receptor complexes were determined by fluorescence recovery after photobleaching (FRAP) experiments as described previously (*66*). A rectangular region of interest (ROI) within the bleached area of the pattern and a rectangular or circular ROI within the bleached area but outside the patterned area were chosen for obtaining intensity values per pixel over time, respectively. Corrected FRAP curves were determined using the following equation:

$$F(t) = \frac{(F_{ROIinside} - F_{offset}) - (F_{ROIoutside} - F_{offset})}{\frac{(F_{ref} - F_{offset})}{(F_{ref,0} - F_{offset})}} \qquad \textit{Eqn. 8}$$

with $F_{\mathrm{ROI,inside}}$ and $F_{\mathrm{ROI,outside}}$ being the fluorescence intensities inside and outside the pattern, respectively, within the bleached spot. F_{ref} is the fluorescence intensity of an unbleached ROI inside the micropattern, and $F_{\mathrm{ref,0}}$ is the fluorescence intensity of this ROI before the bleaching experiment. F_{ref} was implemented as a normalization factor to correct for photobleaching during FRAP experiments. The offset intensity (F_{offset}) was determined from an ROI outside of the cell and was subtracted from all intensity values. Image analysis to obtain corrected FRAP curves was performed using a Matlab script. The corrected FRAP curves F(t) were fitted by a mono-exponential function. Two-sample Kolmogorov-Smirnov-Tests were performed in order to calculate statistical significances.

Atomistic simulation models for JAK2/TpoR

TpoR-ΔECD:JAK2 dimer in a lipid bilayer: System $S1_{AA}$ (Table S4) is an all-atom (AA) model of the JAK2/TpoR homodimer (Fig. 6A, left panel), lacking the ectodomains of TpoR. Two of the known dimerization interfaces; the PK/PK interface of JAK2 (inferred by homology with the X-ray crystal structure of JAK1) and the TM/TM interface of TpoR (initial structure obtained from our simulations $S10_{CG}$-$S13_{CG}$, see description of coarse-grained simulations below), were used to guide the construction of this dimer structure. We first energy minimized the X-ray crystal structure of the FERM-SH2 domain (residues 37-514) of JAK2 (PDB id: 4Z32)(*21*) and then homology modeled the JAK2 PK/PK dimer (residues 526-810) based on the X-ray crystal structure of the JAK1 PK/PK dimer (PDB id: 4L00) (*45*). Next, we linked the PK/PK dimer to the FERM-SH2 domains. In this structure, we aligned the FERM-SH2 domain in an 'upright' orientation, with the F2 subunit of the FERM sub-domain facing the membrane, since it is known to contain an amphipathic region that most likely mediates membrane interactions (*67*). This orients the SH2 sub-domains toward the cytosol, and these were linked to the PK domains through an unstructured linker segment. Since we did not detect intermolecular interactions between the FERM-SH2 domains, they were placed apart from each other. To

complete the full JAK2 dimer structure, we homology modeled the TK domains (residues 811-1132) based on the TYK2 TK domain within the crystal structure of the TYK2 PK-TK fragment (PDB id: 4OLI) (*42*), and concatenated the structures to the PK/PK dimer. For the PK-TK linkage, a flexible and unstructured linker segment was chosen, since in electron microscopy imaging of JAK1 these domains have been observed to exhibit extensive intersegmental flexibility (*68*), and since the TK domains require sufficient flexibility to cross-phosphorylate each other. The assembled JAK2-TpoR dimer complex was then embedded into a pure POPC lipid bilayer using the CHARMM-GUI membrane builder (*69*).

System $S2_{AA}$ is similar to the TpoR-JAK2 dimer complex, but with the V617F mutation. System $S3_{AA}$ is analogous to the $S1_{AA}$ model but embedded into a multicomponent lipid bilayer, containing 70 mol% POPC and 30 mol% cholesterol in its extracellular (EC) leaflet, and 65 mol% POPC, 30 mol% cholesterol, and 5 mol% phosphatidylinositol 4,5-bisphosphate (PI(4,5)P2) in its cytosolic (IC) leaflet.

1:2:2 Epo:EpoR:JAK2 complex in a lipid bilayer: Systems $S4_{AA}$ and $S5_{AA}$ comprise a dimer model of JAK2-EpoR, which was constructed through the following steps. First, we extracted a dimer structure from the tetrameric JAK2 FS-EpoR structure (PDB:6E2Q) and completed the missing loops in both JAK2 and EpoR. The relative orientation of the FERM-SH2 domains corresponding to chains A and C (or B and D) in the 6E2Q structure is close to that of our JAK2-TpoR model (systems $S1_{AA}$-$S3_{AA}$), so we linked the PK and TK domains to the dimeric FS-EpoR structure in a similar fashion to systems $S1_{AA}$-$S3_{AA}$. This places the positively charged patches on the FERM sub-domain close to the membrane: a crucial feature for the proper function of the receptor complex. We then built the TM dimer of EpoR based on the structure of the EpoR TM monomer (PDB:2MV6). The TM/TM interface of EpoR was modeled based on limited structural homology to the TpoR TM/TM interface. We therefore generated two different dimer structures: II-shaped corresponding to System $S4_{AA}$ and X-shaped corresponding to System $S5_{AA}$. Lastly, we linked the structure of the EpoR ectodomains in complex with Epo (PDB:1CN4) to the TM helices to produce the full model of the JAK2-EpoR-Epo dimer (EpoR residues 31-335).

JAK2 PK dimers: Systems $S6_{AA}$ and $S7_{AA}$ are all-atom models of the isolated JAK2 PK/PK dimer corresponding to wild-type and V617F mutant, respectively. The simulation models for these protein complexes were constructed as described above using homology modeling. The mutation was introduced into both of the PK subunits using the MODELLER tool (*70*). These systems were used to explore the importance of the PK/PK interface, and thus were simplified, lacking the rest of the dimer structure (i.e., the TpoR, JAK2 FERM-SH2, and JAK2 TK domains). These isolated PK/PK domain systems were also used to evaluate the binding affinity of the PK/PK interface for different mutants using the MM-PBSA (Molecular Mechanics Poisson-Boltzmann Surface Area) scheme (*71*). Binding affinities were evaluated with the g_mmpbsa tool (*50*), which calculates the enthalpic component of the free energy, assuming changes in the entropic component to be relatively minor. The analysis was conducted at 310 K and the solute dielectric constant was set to 2.5. Snapshots for the analysis were taken at 1 ns intervals. Data were calculated after RMSD-based clustering of the snapshots using a cutoff of 0.25 nm to select the two largest clusters from each simulation.

TpoR TM monomers: Systems $S8_{AA}$ and $S9_{AA}$ are all-atom models of the wt and W515L mutant of the TpoR TM monomers (residues 486-519), respectively. These systems were used to study the tilting of the TM helix in a membrane environment.

TpoR-ΔECD dimers in a lipid bilayer: To construct the TM-TM dimer interface in the JAK2-TpoR homodimer, we modeled the TM domain of TpoR (residues 486-519) based on its structural homology to the TM helix of EpoR (PDB id: 2MV6) (*72*). Since the dimer structure of the TM helices in TpoR is currently unknown, we used coarse-grained (CG) MARTINI

simulations to identify the TM-TM dimer structure (systems $S10_{CG}$-$S13_{CG}$ (Table S4); see description of coarse-grained simulations below). Guided by these CG simulations, an X-shaped dimer structure was selected. This CG dimer structure along with the lipid bilayer was then fine-grained to atomistic representation using one of the CHARMM-GUI tools (*73*). Finally, we homology modeled the intracellular (IC) part of TpoR (residues 520-578) and its binding to the two FERM-SH2 domains of the JAK2 dimer on the basis of the X-ray crystal structures of the closely related JAK1 FS-IFNLR1 (PDB id: 5IXD) (*74*) and TYK2 FS-IFNAR1 complexes (PDB id: 4PO6) (*75*).

Coarse-grained MARTINI simulations

TpoR-ΔECD dimers in a lipid bilayer: To determine the structure of the TM dimer of TpoR, we simulated two TM helices in a POPC bilayer using the CG MARTINI model (*76*). The systems studied correspond to wt ($S10_{CG}$) and the W515L mutant ($S11_{CG}$), respectively (Table S4). The use of CG models enabled modeling over the timescales required to observe spontaneous dimerization in a membrane environment. In both cases, the helices readily dimerized into two different structures: a parallel II-shape and a tilted X-shape. The dimer structures that resulted from the simulations were analyzed and classified according to their residue-by-residue contact maps. Figs. S11 and S12 show the contact maps for the resulting dimers (”X” or ”II”) in both mutant and wt cases, respectively.

In the wt CG simulations (system $S10_{CG}$), seven out of 10 simulations resulted in a parallel II-shaped dimer (see Fig. 1), while the rest were X-shaped dimers (see Fig. S15). In the W515L mutant (system $S11_{CG}$), four out of 10 simulations resulted in an X-shaped dimer while three of the 10 simulations predicted a parallel orientation. Additionally, three simulations showed no dimerization due to insufficient diffusion of the helices. The contact maps (Figs. S15 and S16) illustrate the shape of the dimer and reveal specific interactions in each dimer form. In the X-dimer, for example, H499-H499 interactions are always the most prevalent, while the II-dimer shows contacts throughout the length of the helix. Furthermore, the wt dimers interact via their amphipathic domains, while the W515L mutants do not.

To gain further support for the choice of TM-TM dimer structure, we extracted the most common structures from the last frames of the CG simulations (t = 20 μs) of the systems $S10_{CG}$ and $S11_{CG}$: the X-shaped mutant dimer and the II-shaped wt dimer. We then mutated these TM helices such that the X-shaped W515L mutant became an X-shaped wt (system $S12_{CG}$) and the II-shaped wt became a II-shaped W515L mutant (system $S13_{CG}$). In the simulations of these systems, we found that four of the II-shaped W515L dimers rapidly converted into the X-shape, whereas in the wt case the X-shape persisted. These data suggest that the X-shaped structure is the more stable dimer type, especially in the W515L mutant. It was therefore fine-grained to an all-atom description to complete the atomistic model of the JAK2/TpoR homodimer (system $S1_{AA}$).

TpoR-ΔECD:JAK2 FERM-SH2 monomers in a lipid bilayer: Systems $S14_{CG}$-$S16_{CG}$ comprise a monomeric FERM-SH2 domain bound to the TM and IC domains of TpoR and embedded into a POPC/POPS bilayer (IC leaflet contains 10 mol% of POPS, see Table S4), such that $S14_{CG}$ is a TpoR:JAK2 wt complex, $S15_{CG}$ is a TpoR:JAK2 L224A complex, and $S16_{CG}$ is a TpoR:JAK2 L224E complex. These coarse-grained systems were used to analyze the effect of mutation of the membrane-anchoring L224 residue at longer timescales (20 μs).

Molecular dynamics simulations

Every simulation was initiated with the CHARMM-GUI portal (*73, 77*). This included the CG models and mutations of the TpoR TM helices in the systems $S10_{CG}$-$S16_{CG}$. Interactions in

the simulation systems were described using the all-atom CHARMM36 force field (*78, 79*) or the CG MARTINI model (*76*) (see Table S4). In the all-atom systems, we used the TIP3P water model (*80*). In the CG simulation models, water was described in terms of the MARTINI water beads. In both all-atom and CG descriptions, sodium and chloride ions were added to reach physiological concentration (150 mM), and to neutralize the charge of the system. In the all-atom systems, the ion interactions followed the general CHARMM ion parameters (*81*). Every system was simulated through several repeats to improve sampling (Table S4). The total time scales covered in the simulations were 30 μs (all-atom) and 800 μs (CG simulations).

Simulation Parameters: We employed the GROMACS simulation software package (*82*) to run the simulations. Systems were first energy-minimized and equilibrated for 100 ps with the solute molecules restrained (*77*). Following equilibration, we conducted production runs as described in Table S4. These runs were conducted using the leap-frog integrator with a time step of 2 fs. Periodic boundary conditions were used in all three dimensions. The Verlet lists (*83*) kept track of atomic neighbors and the LINCS algorithm maintained all bonds constrained (*84*). Electrostatic interactions were evaluated with the smooth particle-mesh Ewald (PME) algorithm (*85*) of the order of 4. Lennard-Jones interactions were cut off at 1.2 nm. Temperature was fixed to a physiological 310 K with the Nosé-Hoover thermostat (*86, 87*). Solute and solvent atoms were coupled separately with a time constant of 1 ps. Pressure was coupled isotropically for membrane-exclusive systems and semi-isotropically for the membrane-inclusive systems using the Parrinello-Rahman barostat (*88*) with a time constant of 4 ps. At the beginning of each simulation replicate, random initial velocities were assigned for the atoms from the Boltzmann distribution. Simulation trajectories were saved every 100 ps. For other parameters, GROMACS 5.1.4 defaults (*79, 82*) were used. The CG systems were simulated using the "New-RF" simulation parameters available in Ref. (*89*).

Analysis: Tilt angles between the JAK2 FS domain and the membrane normal were calculated using the *gmx_bundle* tool within GROMACS by defining a vector between the Cα atoms of residues 223 and 492. These residues were chosen to span the principal axis of the FS domain from the membrane anchor within the F2 sub-domain to the tip of the SH2 domain. Fraction of coverage b

y solute (where solute is protein or lipid) for the individual domains of JAK2 within the receptor-JAK2 complex models was obtained by: (i) calculating the solvent accessible surface area (SASA) for each JAK2 domain using the GROMACS *gmx-sasa* tool; (ii) dividing the SASA by the total surface area of each domain to yield the solvent accessible fraction; (iii) subtracting this value from 1.

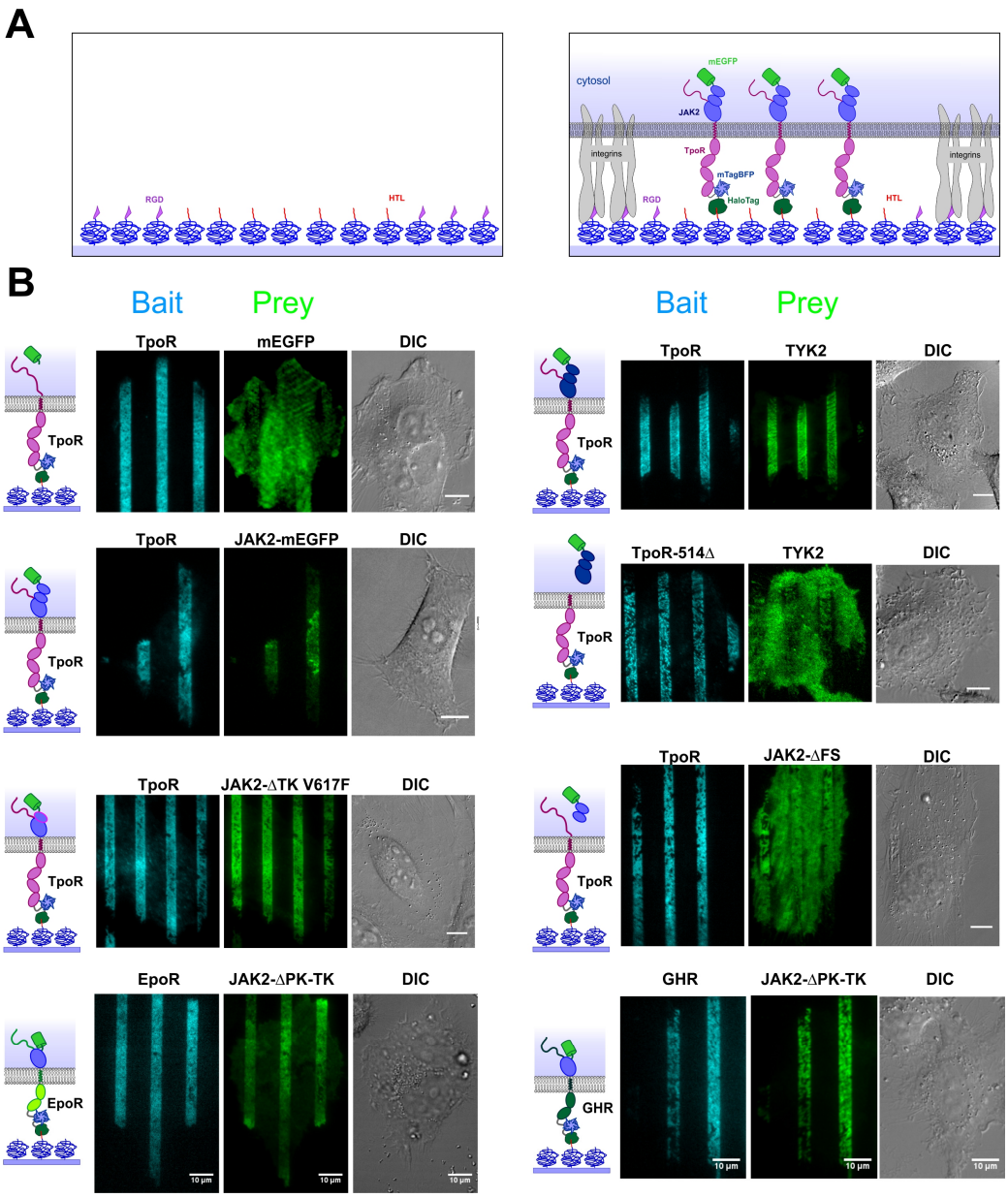

Fig. S1.

Binding of mEGFP-tagged JAK variants to class I cytokine receptors in the plasma membrane probed by live cell micropatterning. (A) Cartoon depicting cell micropatterning: cells expressing TpoR N-terminally fused to the HaloTag and mTagBFP (HaloTag-mTagBFP-TpoR) were cultured on glass coverslips with micropatterned HaloTag ligand (HTL). Upon HaloTag binding to HTL, spatial reorganization of HaloTag-mTagBFP-TpoR (bait) in the plasma membrane is observed. Binding of cytosolic, mEGFP-tagged JAK (prey) proteins to micropatterned TpoR is quantified from the relative contrast of bait and prey proteins. (B) Live cell micropatterning experiments with different micropatterned receptor variants as bait proteins (cyan) and cytosolic mEGFP-tagged (green) JAK variants. Scale bar: 10 µm. DIC: differential interference contrast.

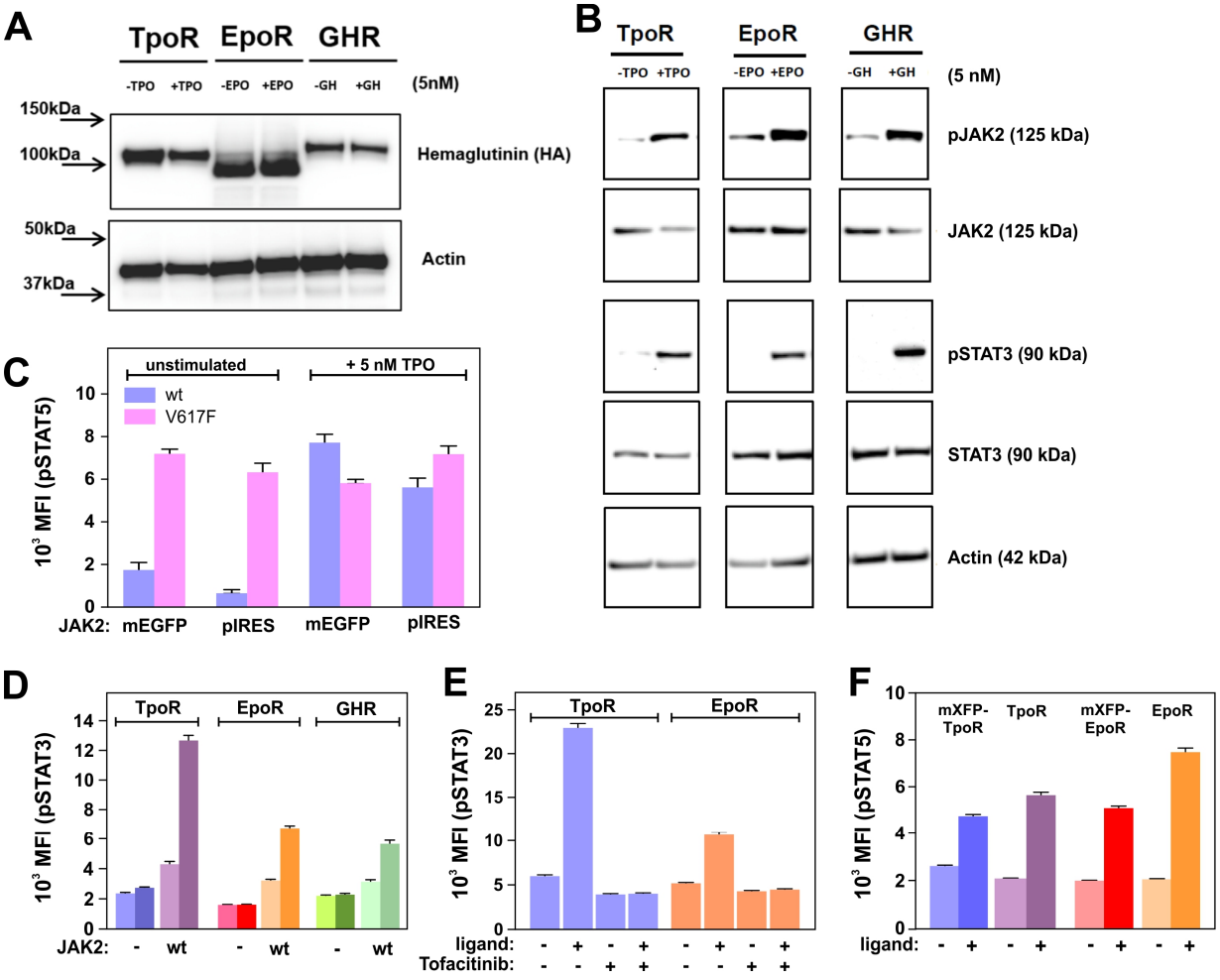

Fig. S2.

Functionality of mXFP-tagged receptors and JAK2 constructs. (A) Expression of mXFP-TpoR, mXFP-EpoR and mXFP-GHR in HeLa cells detected by western blot. (B) Phosphorylation of JAK2 and STAT3 in HeLa clones stably expressing the indicated receptor as detected by western blot. (C) Activity of JAK2-mEGFP (mEGFP) and non-tagged JAK2 (pIRES). HEK293 cells transiently co-transfected with TpoR and JAK2 wt (blue) or V617F (magenta), respectively, were analyzed by phospho-flow cytometry for pSTAT5 without stimulation and after incubating with 5 nM Tpo for 15 min. (D) Ligand-induced STAT3 phosphorylation in cells expressing TpoR, EpoR and GHR as quantified by phospho-flow cytometry. HeLa cells stably expressing the respective receptor were co-transfected with JAK2 and pSTAT3 was quantified in the absence (light color) and presence (dark color) of ligand. (E) STAT3 phosphorylation in cells expressing TpoR and EpoR in the absence and presence of the JAK inhibitor tofacitinib. (F) Comparison of STAT5 activation by mXFP-tagged *vs.* non-tagged TpoR and EpoR. Error bars in (C) – (F) denote SEM.

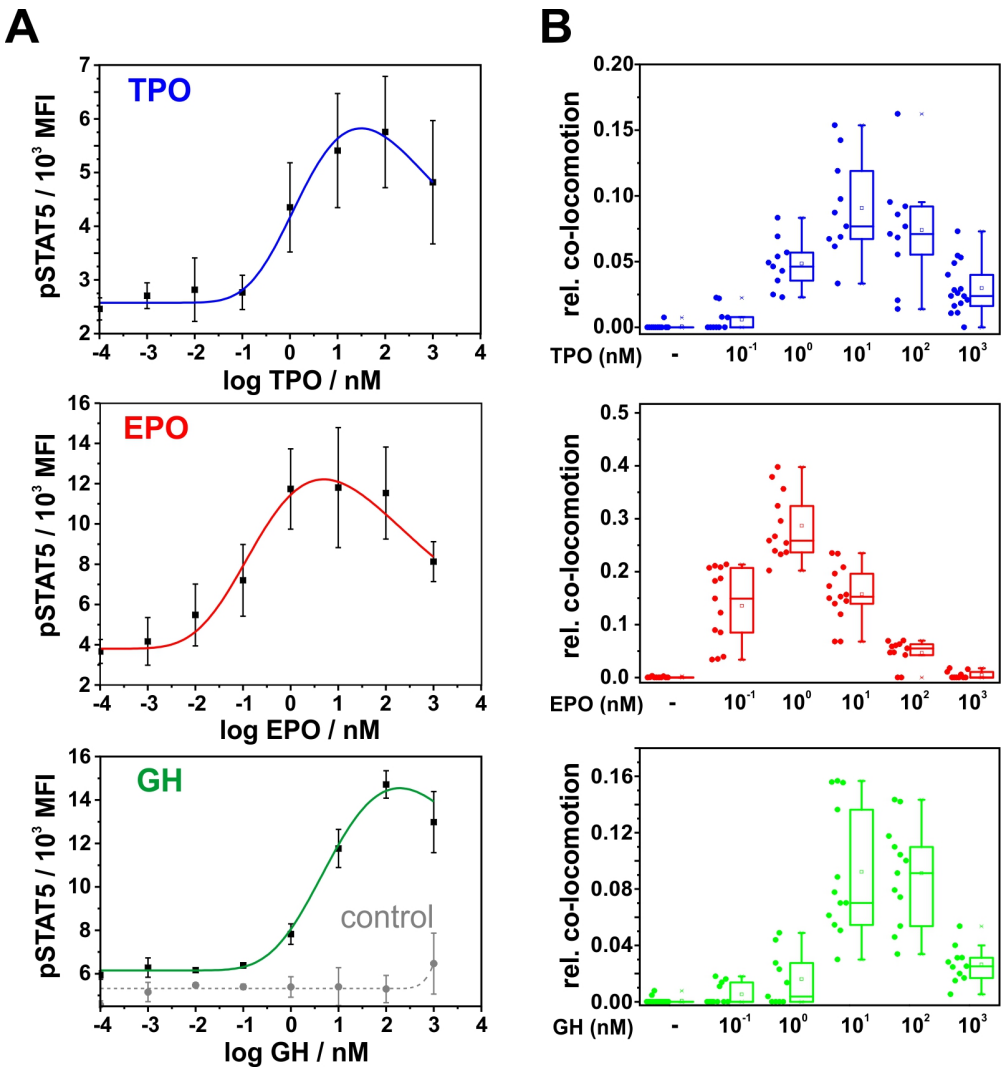

Fig. S3.

Bell-shaped dose-response curves for STAT5 phosphorylation and receptor dimerization. (A) Quantification of phosphorylated STAT5 by phospho-flow cytometry upon ligand stimulation of HeLa clones stably expressing TpoR (top), EpoR (middle) and GHR (bottom). Error bars denote SD from three independent experiments. As a control, parental HeLa cells were analyzed under the same conditions. (B) Ligand concentration-dependent dimerization of TpoR (top), EpoR (middle) and GHR (bottom). Each data point represents the analysis from one cell with a minimum of 10 cells measured for each condition.

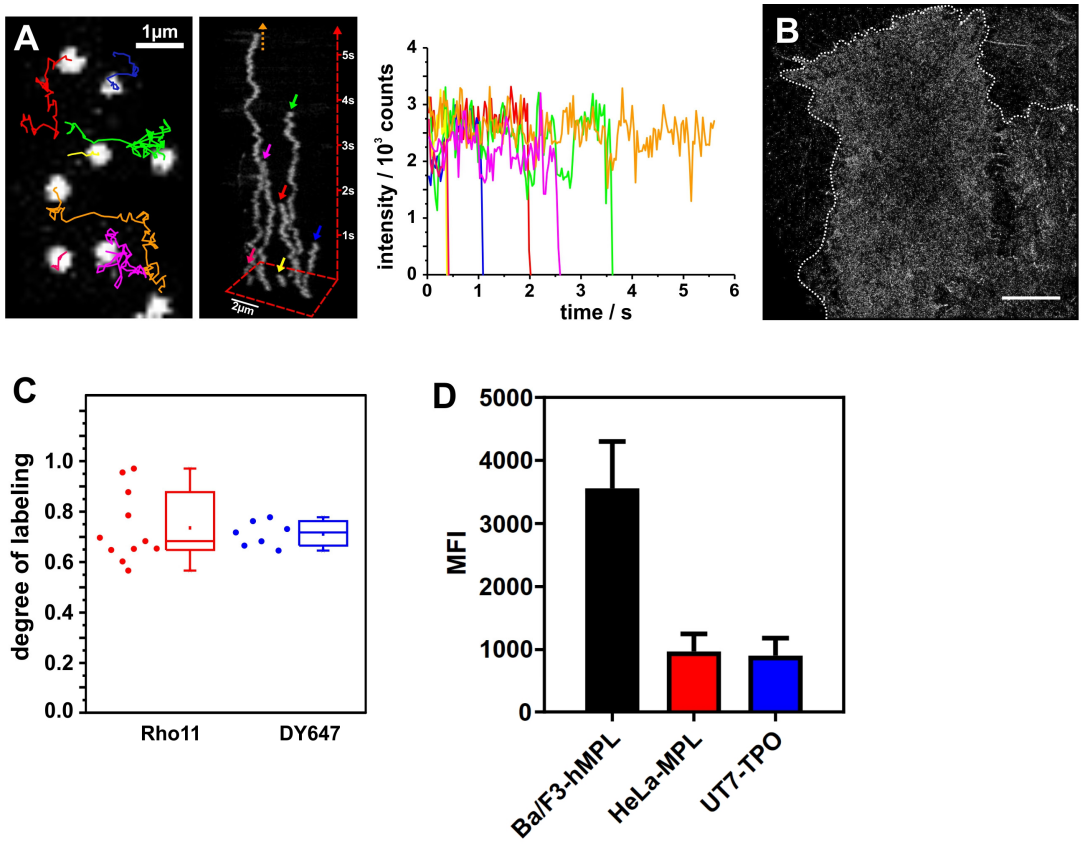

Fig. S4.

Spatiotemporal organization of TpoR in the plasma membrane. (A) Single-step photobleaching of unstimulated TpoR (see Movie S6). Diffusion of individual mXFP-TpoR (^{Rho11}NB) was followed by single particle tracking at elevated laser intensity (561 nm; ~2 mW ≈ 70W/cm²). Trajectories (left), intensity traces (right) and image representation as a pseudo-3D kymograph (center) is shown for seven color-coded particles. (B) Super-resolution images depicting the spatiotemporal cell surface distribution of TpoR in the absence of ligand localized over 16,000 frames. Scale bar: 5 µm. (C) Effective labeling of mEGFP-tagged proteins at the cell surface by anti-GFP nanobodies as quantified by single-molecule co-locomotion analysis. Degree of labelling (DOL) for ^{Rho11}NB was assessed by co-locomotion analysis of SNAPf-mEGFP-IFNAR1 labeled with ^{Rho11}NB and SNAP-Surface 647. DOL for ^{Dy647}NB was assessed by co-locomotion analysis of Halo-mEGFP-IFNAR2 labeled with ^{Dy647}NB and HaloTag ligand-conjugated tetramethylrhodamine (HTL-TMR). Each data point represents the analysis from one cell. (D) Quantification of TpoR cell surface expression levels in different cell lines by flow cytometry and staining with fluorescence-labeled Tpo (50 µg/mL). Error bars denote SD from three independent experiments.

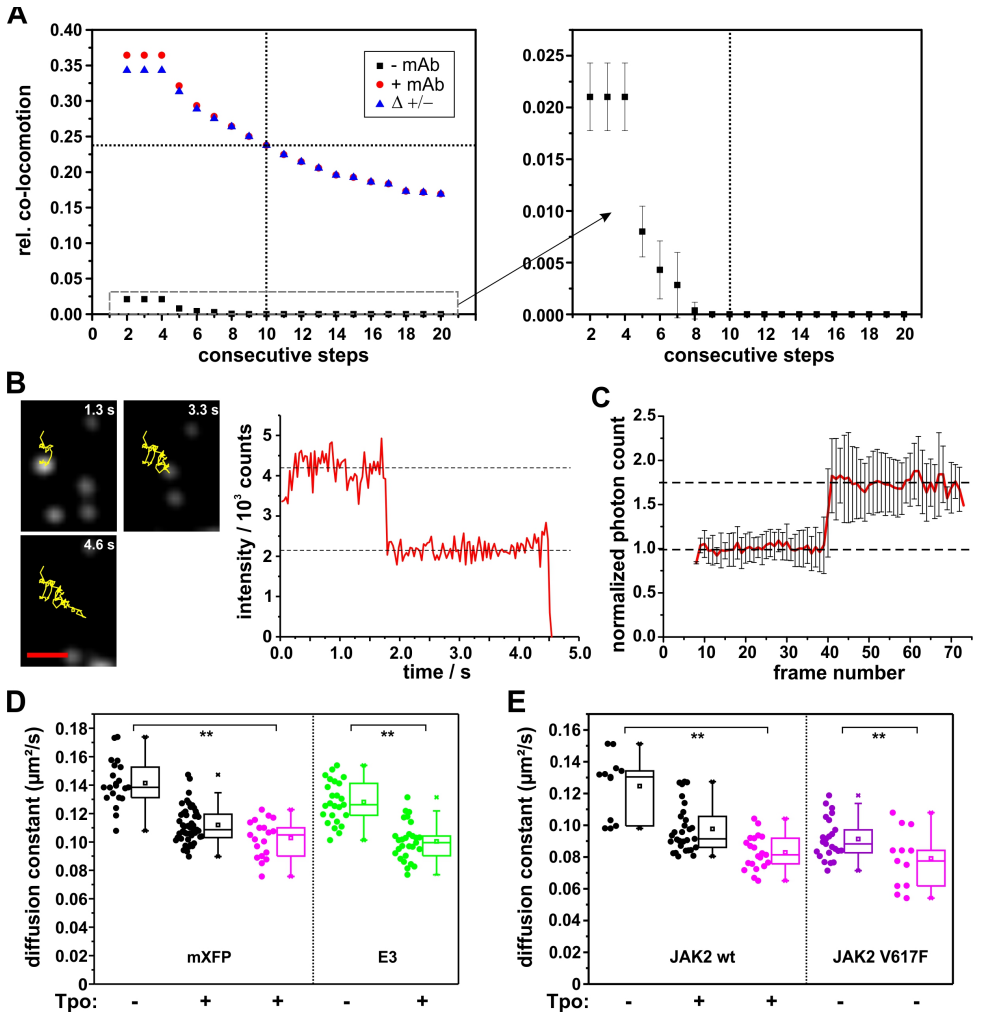

Fig. S5.

Quantitative TpoR dimerization analysis. (A) Co-locomoting fractions obtained upon using different numbers of consecutive steps as a cut-off for co-tracking analysis. Comparison for mEGFP-MBP-TMD in the absence (negative control, black squares) and presence (positive control, red circles) of a monoclonal anti-MBP IgG (mAb) and enlarged view of the dashed rectangle showing the negative control (right). Error bars denote SD from >10000 particles. (B) Dual-step photobleaching within a TpoR trajectory indicating dimer formation in the presence of Tpo. Scale bar: 1 µm. (C) Receptor dimerization detected by single molecule FRET: increase in Rho11 fluorescence (FRET donor) upon photobleaching of DY647 (FRET acceptor) within individual receptor dimers. Mean normalized intensity from 14 trajectories aligned for photobleaching of DY647 at frame number 40. The average increase in donor intensity of 75% corresponds to a FRET efficiency of 43%. (D) Comparison of the diffusion constants for mXFP-tagged and E3-tagged TpoR in the absence and presence of Tpo as obtained from single molecule trajectories. Diffusion constants obtained from co-trajectories are highlighted in magenta. (E) Diffusion of mXFP-tagged TpoR co-expressed with JAK2 wt (black) and V617F (violet), respectively. Diffusion constants obtained from co-trajectories are highlighted in magenta. In (D) and (E), each data point represents the analysis from one cell with a minimum of 10 cells measured for each condition. ** $P \leq 0.01$.

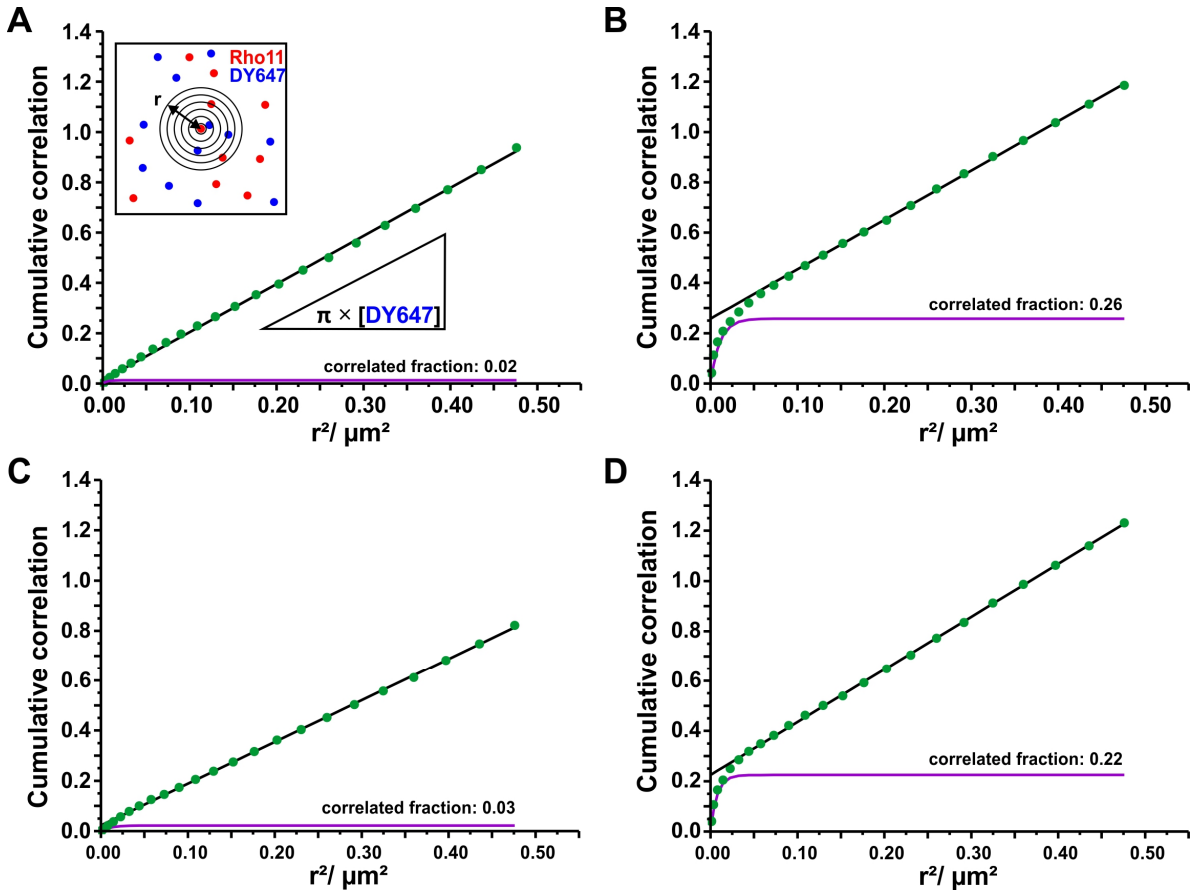

Fig. S6.

Spatial receptor organization in the plasma membrane quantified by particle image cross-correlation spectroscopy (PICCS). (A, B) PICCS analysis for a dual-color labeled model transmembrane protein in the absence (A) and presence (B) of a dimerizing monoclonal antibody. (C, D) PICCS analysis for unstimulated (C) and Tpo-stimulated (D) TpoR. green dots: cumulative correlation function obtained from single-molecule localizations. Black line: linear contribution of the cumulative correlation function. Purple line: cumulative correlation after subtraction of the linear term (black line). The curves show representative data from individual cells. Full statistical analysis is summarized in Table S2.

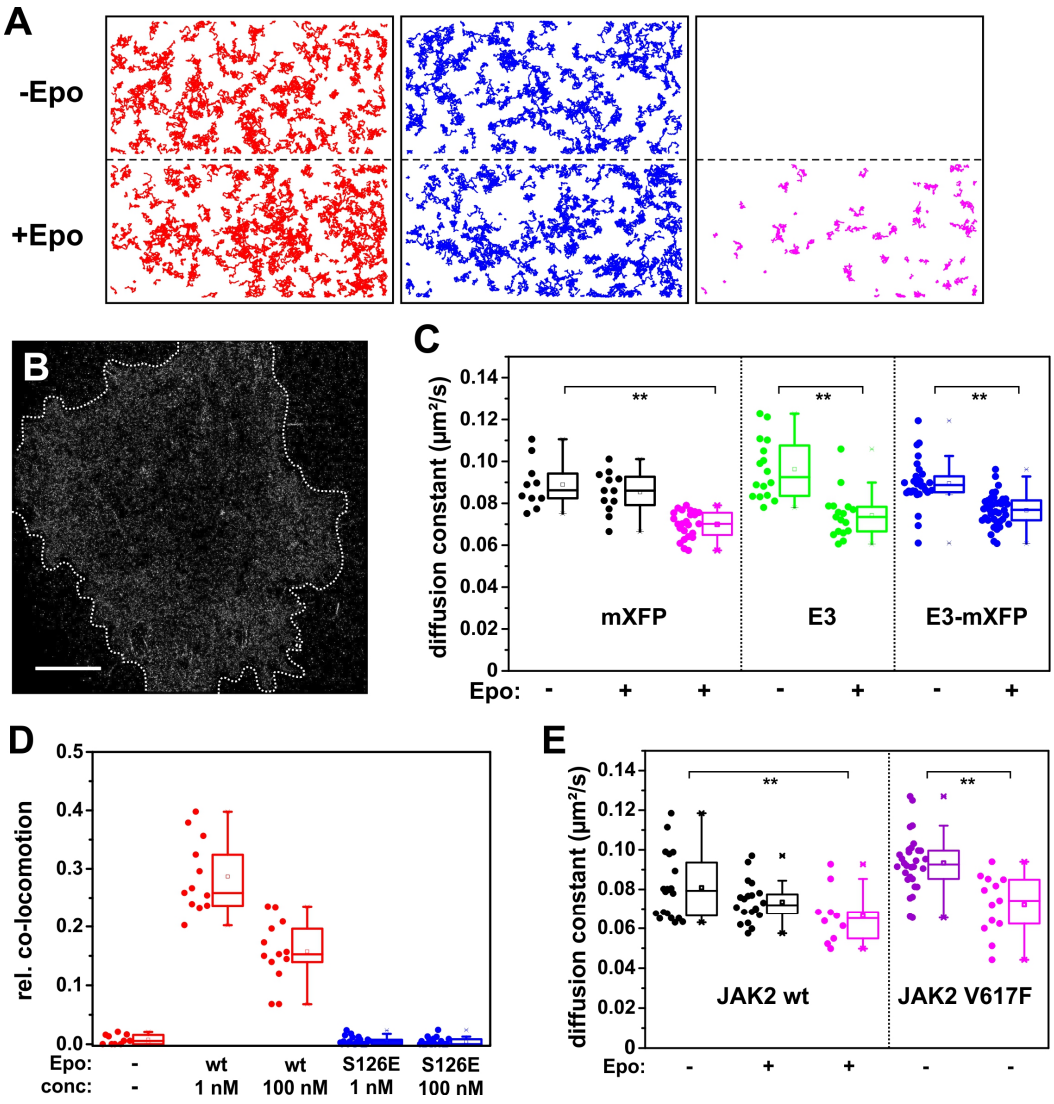

Fig. S7.

Dimerization and spatiotemporal organization of EpoR. (A) Dual color co-tracking of EpoR in the absence (top) and presence (bottom) of Epo. Trajectories (150 frames, ~4.8 s) of individual ^{Rho11}NB-labeled (red) EpoR, ^{DY647}NB-labeled (blue) EpoR, and co-trajectories (magenta) are shown for a representative cell. (B) Super-resolution images depicting the spatiotemporal cell surface distribution of EpoR in the absence of ligand localized over 16,000 frames. Scale bar: 5 µm. (C) Comparison of the diffusion constants for mXFP-tagged, E3-tagged and E3-mXFP-tagged EpoR in the absence and presence of Epo. Diffusion constants obtained from co-trajectories are highlighted in magenta. (D) Dimerization of EpoR by Epo wt (red) and S126E (blue) applied at two different concentrations. (E) Diffusion of mXFP-tagged EpoR co-expressed with JAK2 wt (black) and V617F (purple), respectively. Diffusion constants obtained from co-trajectories are highlighted in magenta. In (C), (D) and (E), each data point represents the analysis from one cell with a minimum of 10 cells measured for each condition. **P ≤ 0.01.

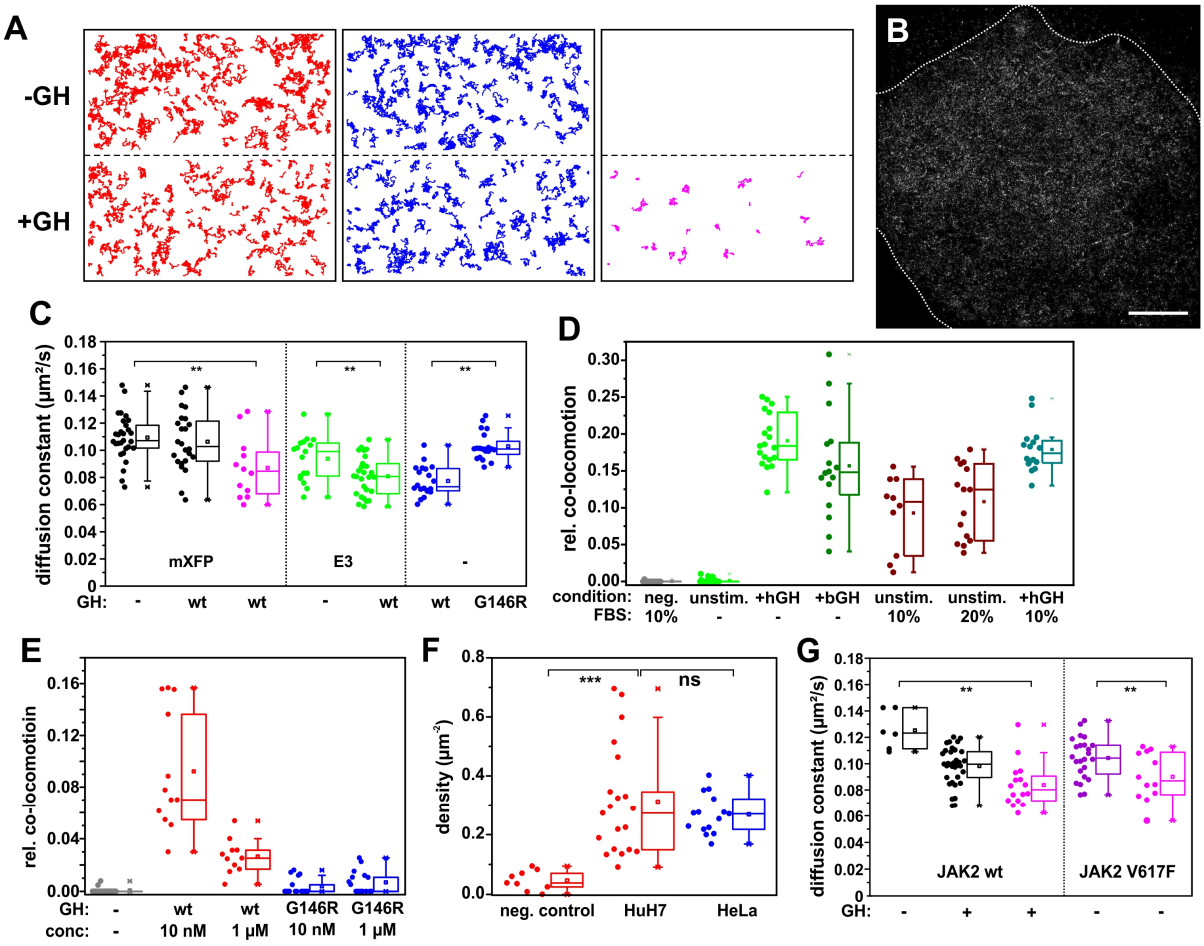

Fig. S8.

Spatiotemporal organization and dynamics of GHR. (A) Dual color co-tracking of GHR in the absence (top) and presence (bottom) of GH. Trajectories (150 frames, ~4.8 s) of individual ^{Rho11}NB-labeled GHR (red), ^{DY647}NB-labeled GHR (blue), and co-trajectories (magenta) are shown for a representative cell. (B) Super-resolution images depicting the spatiotemporal cell surface distribution of GHR in the absence of ligand localized over 16,000 frames. Scale bar: 5 µm. (C) Diffusion constants of mXFP-tagged (black) and E3-tagged (green) GHR in the absence and presence of GH. For comparison, diffusion of fluorescently-labeled GH wt and G146R bound to non-tagged GHR expressed in HeLa cells was determined (blue). Diffusion constants obtained from co-trajectories are highlighted in magenta. (D) Serum-starving is critically required for background-free dimerization experiments with GHR. Co-locomotion analysis of GHR transfected cells was measured for unstimulated cells and after stimulation with the indicated ligand (5 nM, 10 min) either for cells cultured in FBS-containing media (10%) or after serum starvation and scavenging of residual bovine GH with the ectodomain of GHR (-). Wt JAK2-mEFGP was co-expressed in all tested conditions. (E) Comparison of GHR dimerization by GH wt (red) and G146R (blue) at two different concentrations. (F) Density of endogenous GHR in HuH7 cells compared to stably transfected HeLa cell lines as quantified by incubating with 10 nM ^{DY648}GH. 10 nM ^{DY648}GH mixed with 100 nM unlabeled GH was used as a negative control. (G) Diffusion of mXFP-tagged GHR co-expressed with JAK2 wt (black) and V617F (purple), respectively. Diffusion constants obtained from co-trajectories are highlighted in magenta. In (C) - (G), each data point represents the analysis from one cell with a minimum of 10 cells measured for each condition. **P ≤ 0.01; ***P ≤ 0.001; ns, not significant.

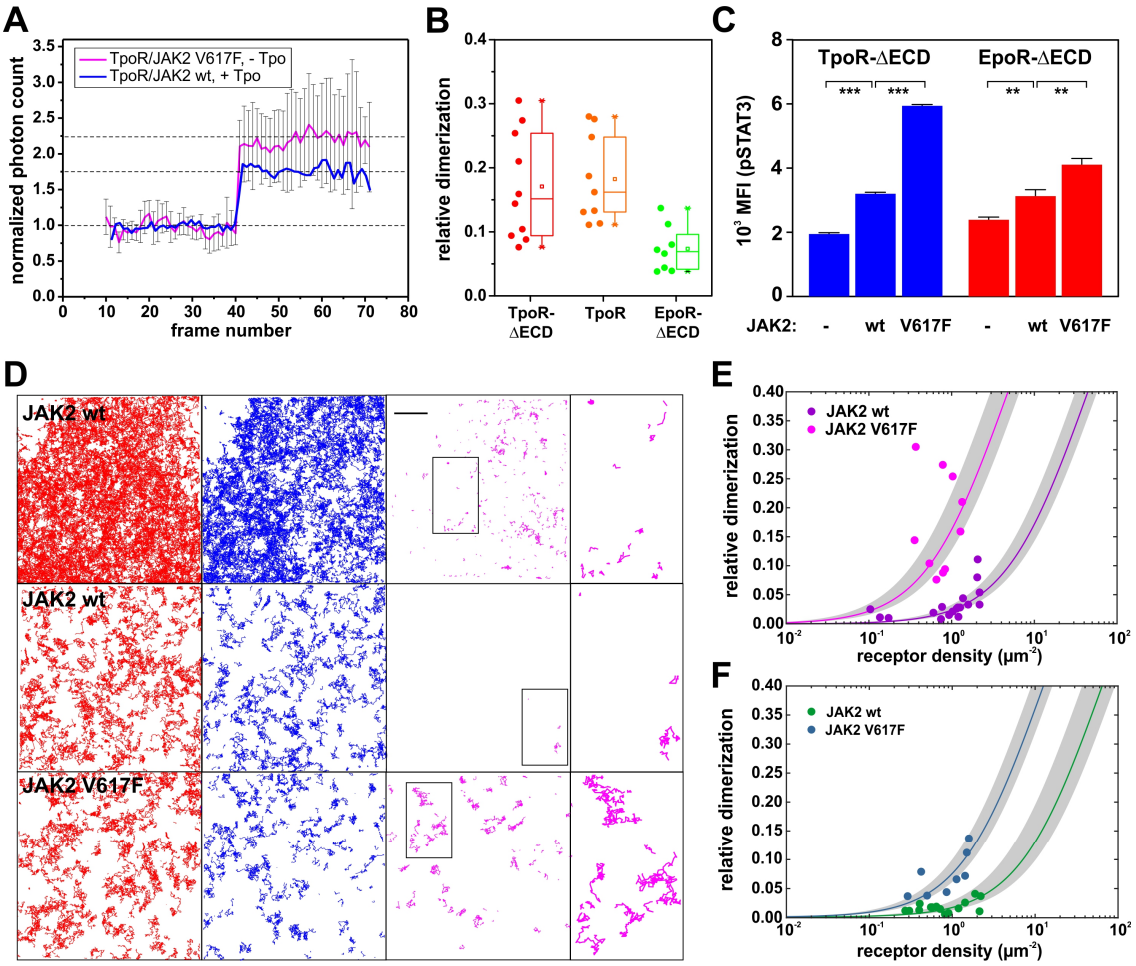

Fig. S9.

Ligand-independent dimerization and activation of TpoR in the presence of JAK2 V617F. (A) TpoR dimerization detected by single-molecule (sm) FRET: increase in Rho11 fluorescence intensity upon photobleaching of DY647 within individual receptor dimers, imaged at elevated laser intensities to induce acceptor photobleaching. Relative changes in donor intensities for ligand-independent TpoR dimers in the presence of JAK2 V617F (magenta curve) and for TpoR co-expressed with wt JAK2 and dimerized by Tpo (blue curve). Mean normalized intensities calculated from ≥10 trajectories that were aligned for photobleaching of DY647 at frame number 40 are shown. Error bars denote SD. (B) Ligand-independent dimerization of TpoR, TpoR-ΔECD and EpoR-ΔECD in the presence of JAK2 V617F quantified by smFRET. (C) Ligand-independent activation of TpoR-ΔECD (blue) and EpoR-ΔECD by JAK2 wt and V617F. Error bars denote SEM. Significances of $P \leq 0.01$ and $P \leq 0.001$ are indicated by ** and ***, respectively. (D) Representative smFRET experiments with TpoR co-expressed with JAK2-mEGFP wt (top and middle rows) and V617F (bottom row) showing single molecule trajectories of the donor (red) as well as the acceptor upon direct excitation (blue) and via smFRET (magenta) detected over 150 frames (5 s). Total receptor densities were 1.2/μm² (top row) and 0.6/μm² for JAK2 wt (middle row) as well as 0.4/μm² for JAK2 V617F (bottom row). Selected regions with co-trajectories are enlarged in the panel at the right. Scale bar: 5 μm. (E, F) Ligand-independent dimerization of TpoR-ΔECD (E) and EpoR-ΔECD (F) in the presence of JAK2 wt and V617F observed by smFRET. The law of mass action for a monomer-dimer equilibrium was fitted (solid lines) with the confidence intervals indicated as grey zones.

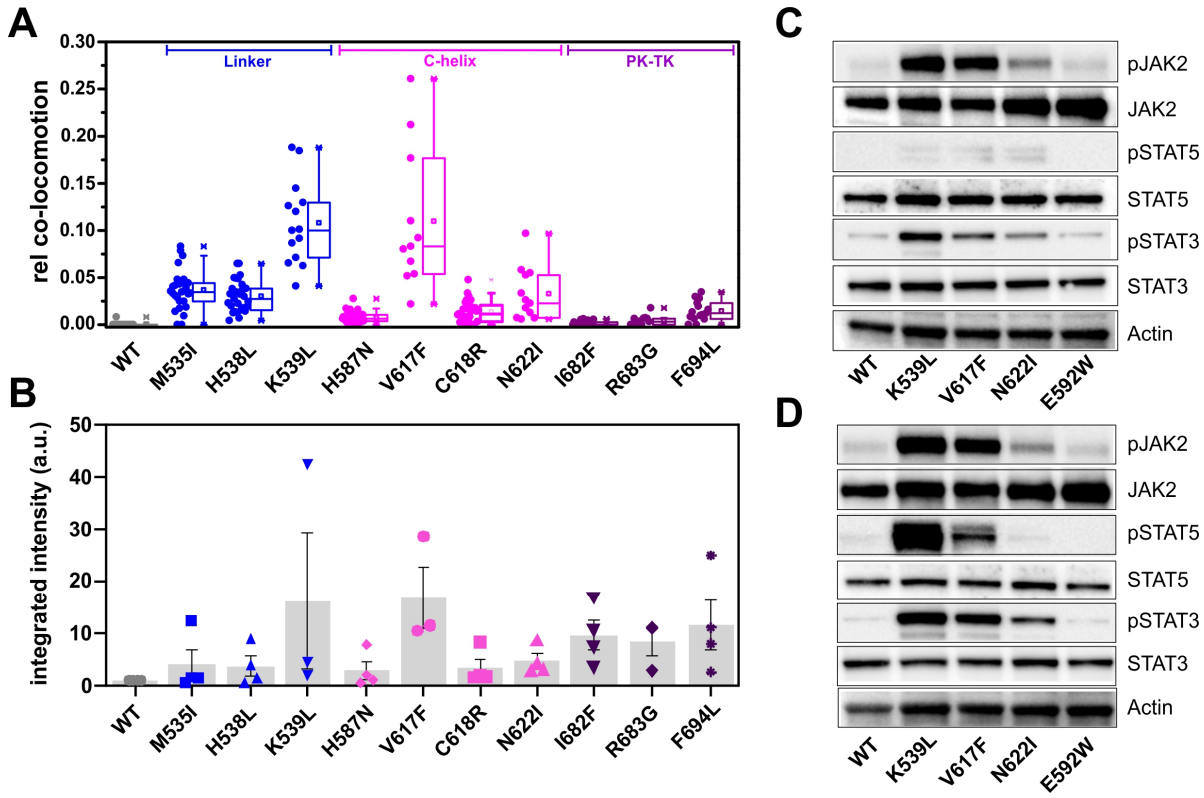

Fig. S10.

Activation of TpoR, EpoR and GHR by oncogenic JAK2 mutants located in the PK domain. (A, B) Comparison of ligand-independent dimerization (A) and JAK2 phosphorylation (B) observed upon co-expression of JAK2 wt and oncogenic mutants with TpoR. In (A), each data point represents the analysis from one cell with a minimum of 10 cells measured for each condition. In (B), the grey columns indicate mean intensity values from four independent phospho-JAK2 blots, which are represented as data points. Error bars denote SEM from four independent experiments. (C, D) Representative western blots showing ligand-independent JAK/STAT phosphorylation observed for JAK2 wt and selected dimerizing mutants co-expressed with EpoR (C) and GHR (D).

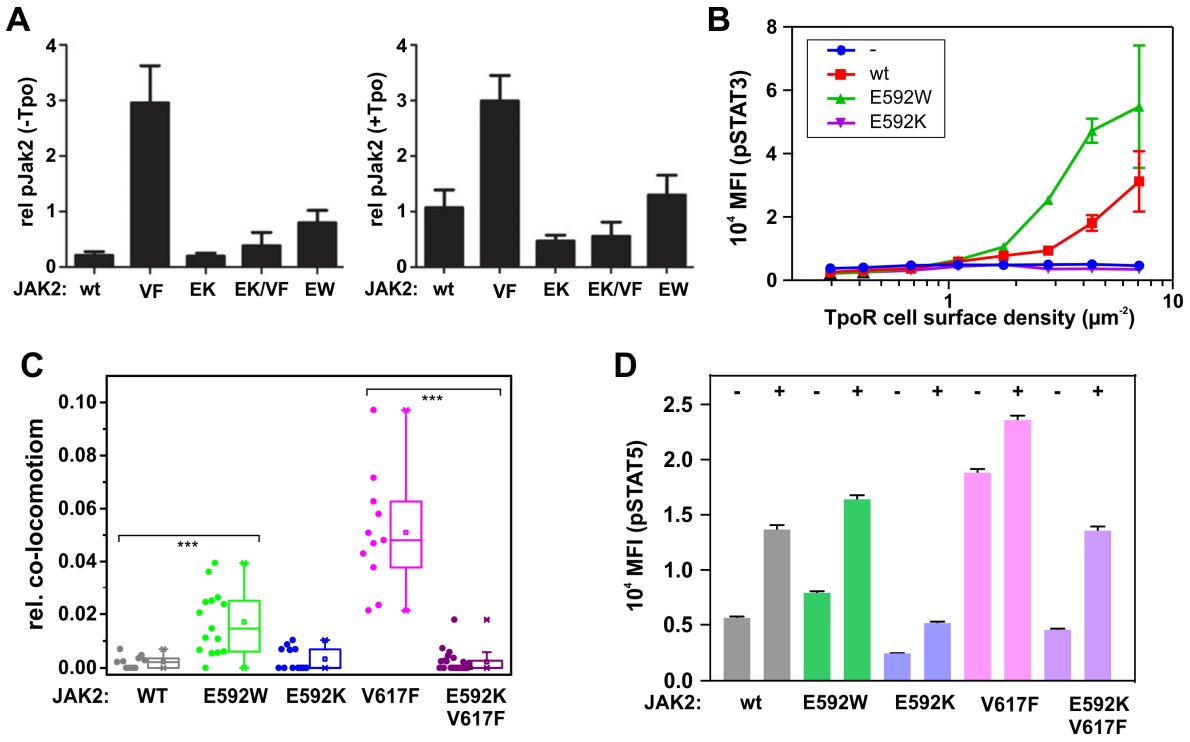

Fig. S11.

Role of the putative JAK2 PK-PK interface probed by mutating E592. (A) Phosphorylation of JAK2 wt and mutants V617F (VF), E592K (EK), EK/VF and E592W (EW) co-expressed with TpoR in the absence (left) and presence (right) of Tpo as determined densitometrically from western blots. Error bars denote SD from three independent experiments. (B) Receptor density-dependent activation of TpoR by JAK2 wt, E592W and E592K in the absence of Tpo. Error bars denote SEM. (C, D) Ligand-independent EpoR dimerization (C) and STAT5 phosphorylation (D) induced by JAK2 mutations. STAT5 phosphorylation was probed by phospho-flow cytometry of HeLa cells stably expressing EpoR. JAK2 wt and mutants were transiently expressed and pSTAT5 was quantified in the absence (-) and presence (+) of Epo. In (C), each data point represents the analysis from one cell with a minimum of 10 cells measured for each condition. ***$P \leq 0.001$. Error bars in (D) denote SEM.

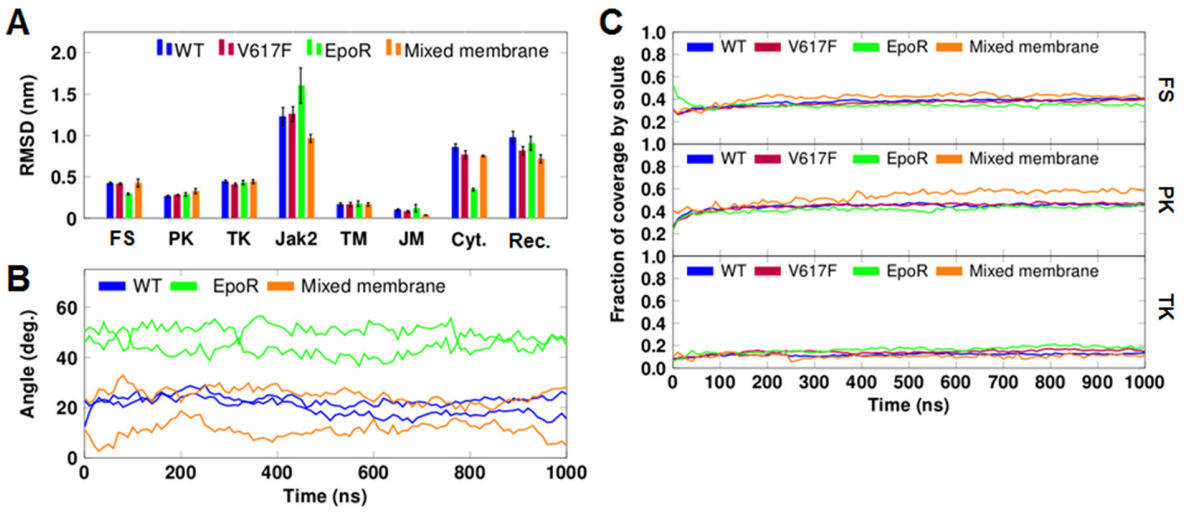

Fig. S12.

Comparison of the atomistic MD simulations for TpoR and EpoR under different conditions. (A) Root-mean-square deviations (RMSDs) of different protein domains and whole proteins observed in different MD simulations: TpoR/JAK2 wt in POPC (blue); TpoR/JAK2 V617F in POPC (red); EpoR/JAK2 wt in POPC (green); TpoR/JAK2 wt in POPC/PI(4,5)P_2/cholesterol (orange). TM: transmembrane helix residues (TpoR: 492—513; EpoR: 251—273); JM: juxtamembrane region residues (TpoR: 514-517; EpoR: 273-277); Cyt.: the remaining cytoplasmic residues; Rec.: entire receptor. Error bars denote SEM. (B) Tilt angle of the FERM-SH2 domain with respect to the membrane normal. We calculated this tilting angle by defining a vector between the C_α atoms of residues 223 and 492 and comparing it to the membrane normal with the GROMACS tool *gmx bundle*. These residues were chosen to span the principal axis of the FS domain from the membrane-anchoring part of the F2 FERM subdomain to the tip of the SH2 domain. The EpoR systems display an orientation of the FERM-SH2 domain that is tilted an additional 20—30 degrees compared to the TpoR systems due to a more tilted initial dimer pose in the 6E2Q template structure. Same color coding as in A. (C) Fraction covered by solute for three JAK2 domains (FS (top); PK (middle); TK (bottom)) in four different systems. This estimates how much the surface of each domain is covered by solute (*i.e.* protein or membrane components). The data are obtained by combining simulation replicates of systems $S1_{AA}$-$S5_{AA}$. Same color coding as in A.

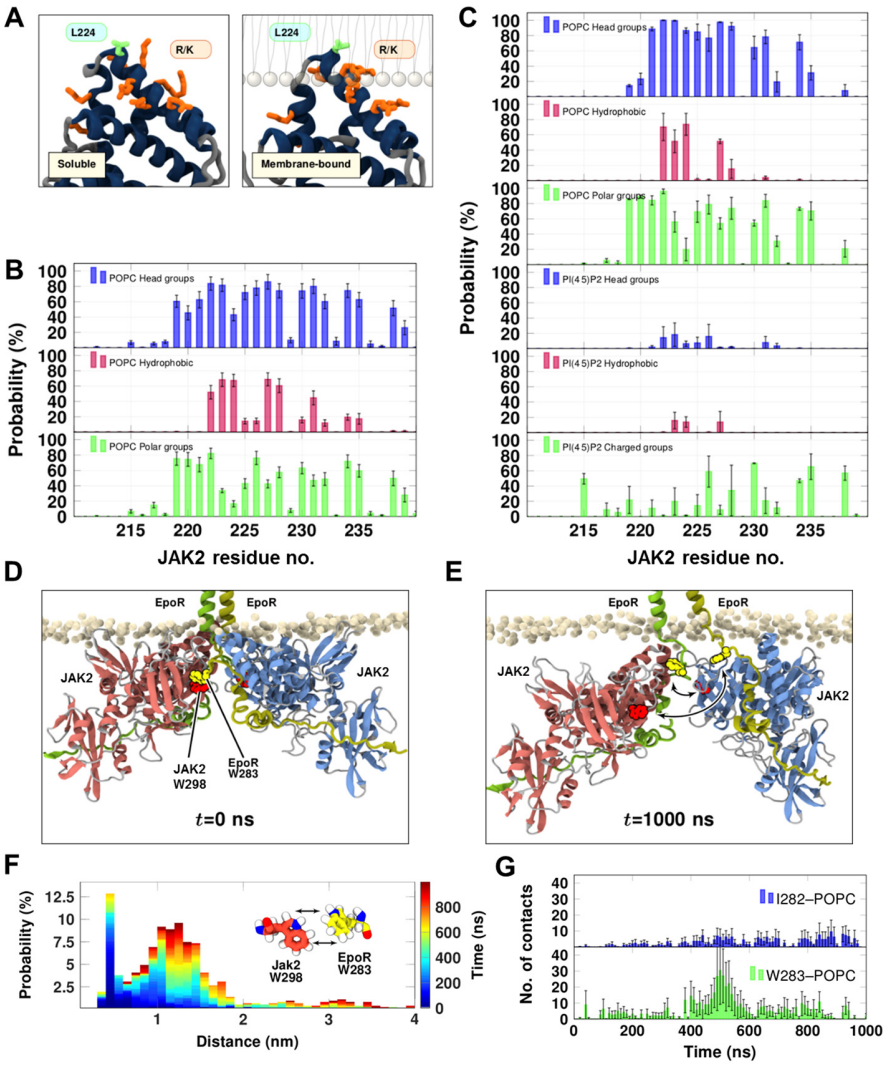

Fig. S13.

JAK2 organization at the membrane explored by MD simulations. (A) Membrane anchoring of JAK2 FERM F2 subdomain (system *S1*$_{AA}$) induces a conformational reorganization of L224 (green). (B, C) Probability of contacts between residues of the F2 subdomain of FERM and different structural elements of the lipid bilayer, as obtained for a neutral pure POPC membrane (B) and for a negatively charged membrane (65 mol% POPC, 30 mol% cholesterol and 5 mol% phosphatidylinositol-4,5-bisphosphate) (C). Data are calculated from systems *S1*$_{AA}$ and *S3*$_{AA}$, respectively. Error bars denote SEM. (D-G) Behavior of the membrane proximal EpoR residues (I282 and W283) responsible for the dimerization of JAK2 FS domains in the PDB:6E2Q structure. (D, E) Snapshots at the (D) beginning (t = 0) and (E) end (t = 1000 ns) of a simulation. EpoR W283 (yellow) and JAK2 W298 (red) are highlighted. The arrows highlight the dissociation of EpoR W283 from the dimerization pocket. The JAK2 PK and TK domains have been omitted for clarity. (F) Minimum distance histogram calculated between EpoR W283 and JAK2 W298 and color-coded to indicate the simulation time. The initial state corresponds to the highest probability peak at a distance of ~0.4 nm. (G) Numbers of contacts between the membrane proximal EpoR residues (I282 and W283) and POPC lipids during the simulation. Errors represent standard error of the mean (SEM). Data are calculated from systems *S4*$_{AA}$ and *S5*$_{AA}$, comprising four simulation replicates.

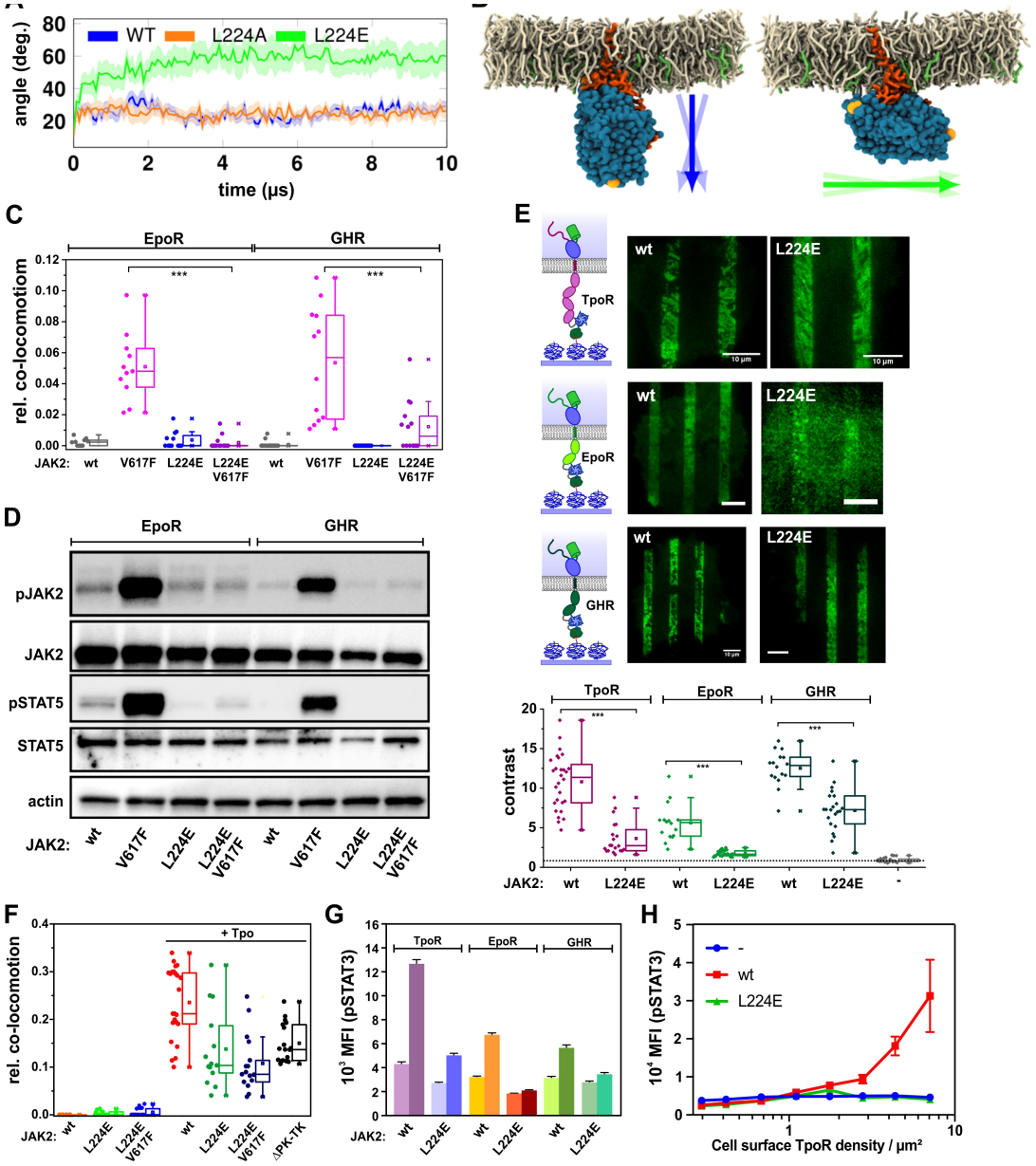

Fig. S14.

The mutation L224E in the JAK2 FERM domain affects structural organization and activity. (A, B) Orientation of the JAK2 FERM-SH2 domain at the plasma membrane upon introduction of the JAK2 mutations L224A and L224E as determined from MD simulations (A) as outlined by the arrows in the snapshots from MD simulations of JAK2 wt (left, system *S14*$_{CG}$) and L224E (right, system *S16*$_{CG}$). Arrows indicate the orientation of the FS domain and its variation during the simulations. (C, D) Ligand-independent dimerization (C) and JAK2 phosphorylation (D) upon co-expression of EpoR and GHR, respectively, with different JAK2 mutants. (E) Receptor binding of JAK2 wt and L224E confirmed by cell micropatterning. Representative images obtained for JAK2 FS wt and L224E fused to mEGFP interacting with micropatterned TpoR, EpoR and GHR, respectively, and comparison of the contrast (bottom). The contrast obtained for the negative control with mEGFP as prey protein ("-") is indicated by the dotted line. (F) Dimerization of TpoR co-expressed with different JAK2 mutants in the absence and presence of Tpo. (G, H) Activity of JAK2 L224E probed by phospho-flow cytometry of pSTAT3. (G)

Ligand-induced STAT3 phosphorylation in cells co-expressing TpoR, EpoR or GHR with JAK2 wt or L224E. Light color: no stimulation; dark color: stimulation with 10 nM cytokine for 15 min. (H) Receptor-density dependent STAT3 phosphorylation upon co-expression of TpoR with JAK2 wt and L224E in the absence of Tpo. In (C), (E) and (F) , each data point represents the analysis from one cell with a minimum of 10 cells measured for each condition. Significances of $P \leq 0.001$ are indicated by ***. Error bars in (G) and (H) denote SEM.

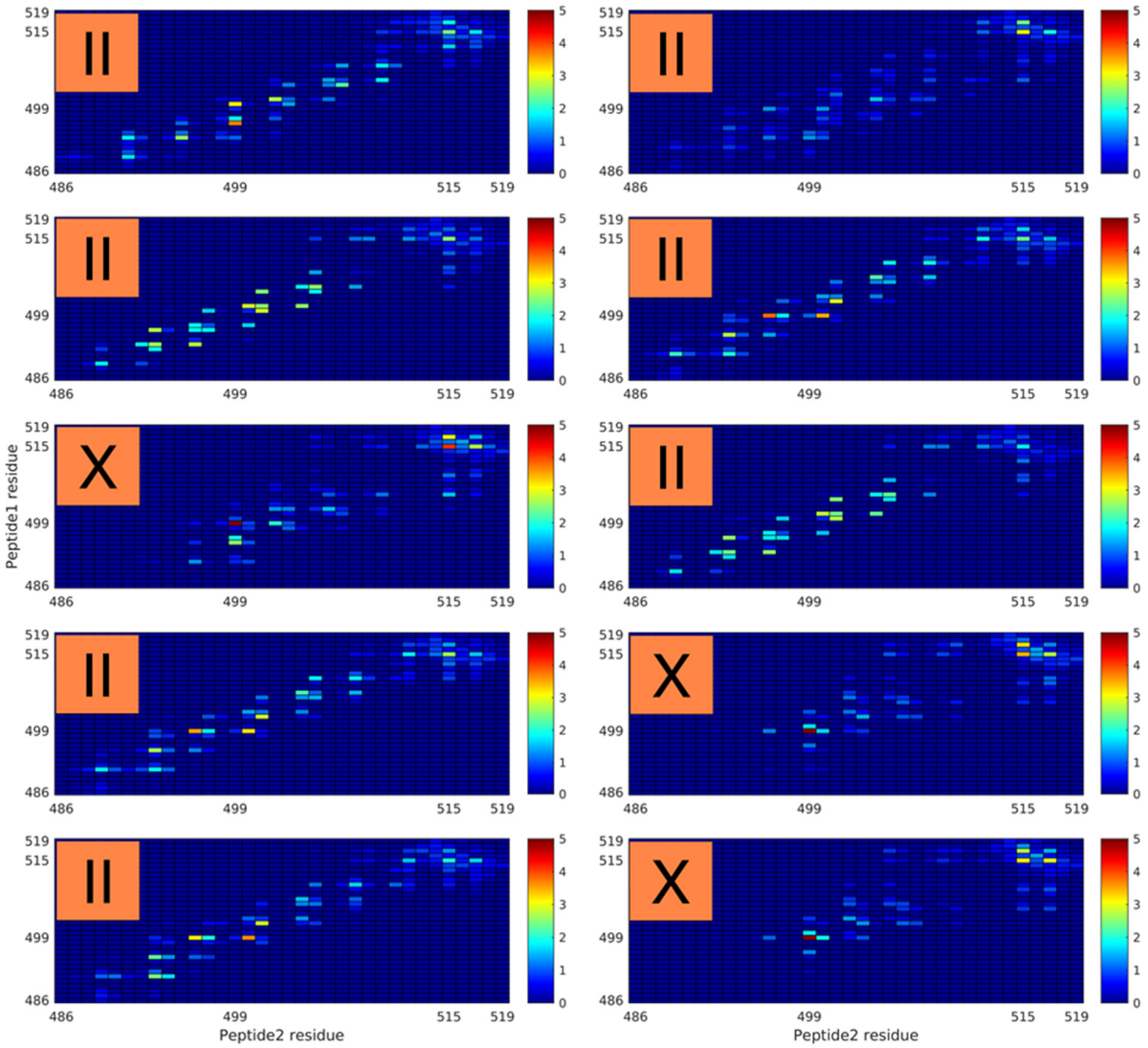

Fig. S15.

Contact profiles in the TM-JM segments of wild-type TpoR dimers (calculated from the system *S10*$_{CG}$). Residues from helix 1 are shown along the y-axis and those from helix 2 along the x-axis. Color bar indicating the average number of contacts is shown on the right. Contacts were calculated with the GROMACS tool *gmx mindist*: a contact was counted if two residues were within a distance of 0.6 nm. The upper left panel indicates the prevailing dimer configuration in the simulation. ”II” denotes a parallel configuration for the two TM helices, whereas ”X” represents tilted TM helices in the dimer.

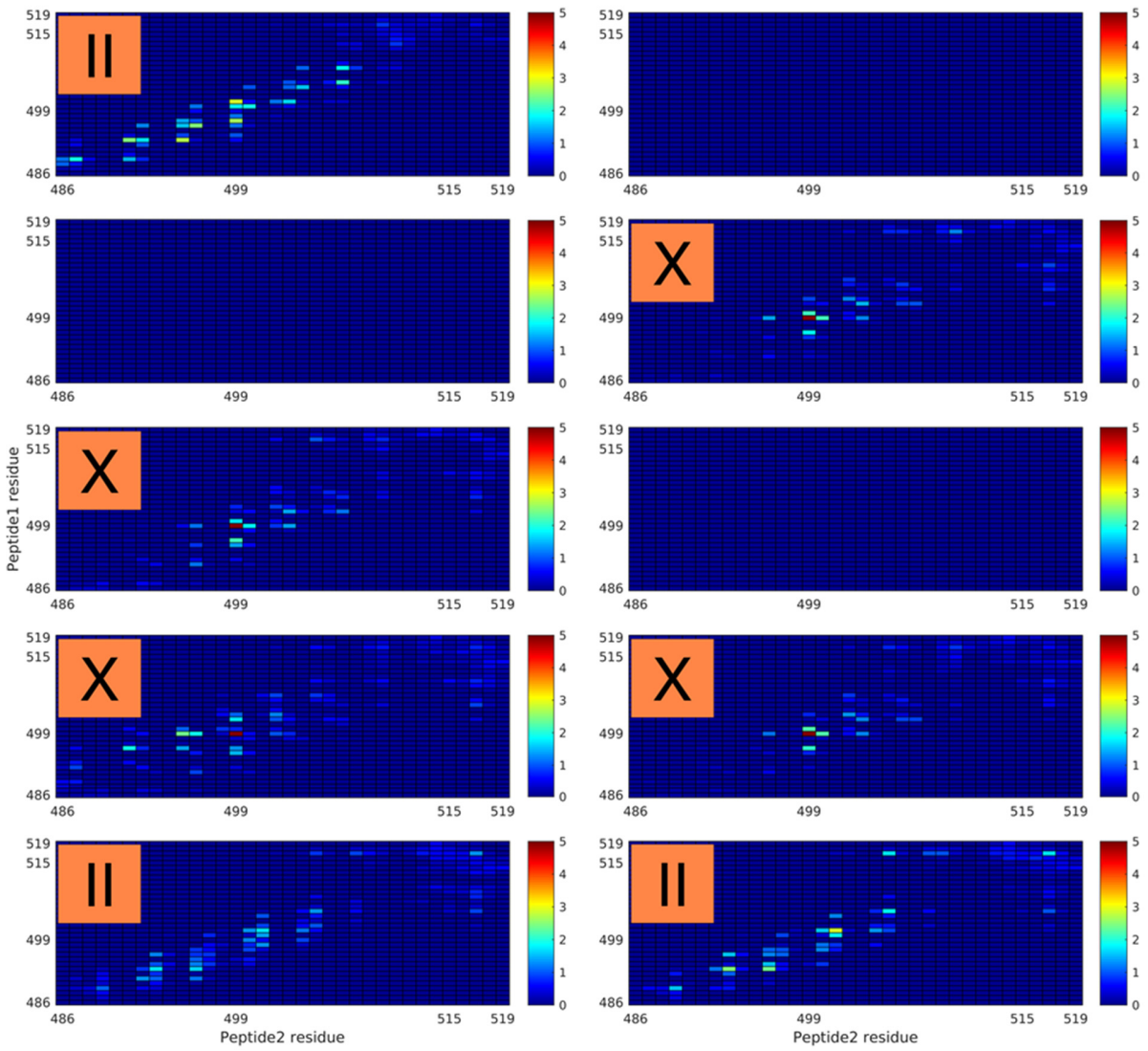

Fig. S16.

Contact profiles in the TM-JM segments of W515L TpoR dimers (calculated from the system *S11*$_{CG}$). Residues from helix 1 are shown along the y-axis and those from helix 2 along the x-axis. Color bar indicating the average number of contacts is shown on the right. Contacts were calculated with the GROMACS tool *gmx mindist*: a contact was counted if two residues were within a distance of 0.6 nm. The upper left panel indicates the prevailing dimer configuration in the simulation. ”II” denotes a parallel configuration for the two TM helices, whereas ”X” represents tilted TM helices in the dimer.

Table S1.

Diffusion constants and fractions of immobile particles of TpoR, EpoR and GHR under different conditions.

Receptor	JAK2	Ligand	D [µm²/s][a]	D [µm²/s][b]	D [µm²/s][c]	D [µm²/s][d]	Immob.[e]
MBP-TMD	-	-	0.142 ± 0.008	-	-		0.066 ± 0.022
MBP-TMD	-	mAb	0.081 ± 0.012	0.079 ± 0.018	-		0.147 ± 0.067
TpoR	-	-	0.141 ± 0.016	-	0.128 ± 0.014		0.081 ± 0.025
TpoR	wt	-	0.124 ± 0.019	-	-		0.062 ± 0.021
TpoR	-	Tpo	0.112 ± 0.013	0.102 ± 0.012	0.100 ± 0.013		0.104 ± 0.033
TpoR	wt	Tpo	0.097 ± 0.014	0.082 ± 0.010	-		0.096 ± 0.062
TpoR	V617F	-	0.091 ± 0.012	0.079 ± 0.018	-		0.114 ± 0.043
EpoR	-	-	0.088 ± 0.011	-	0.096 ± 0.014		0.361 ± 0.088
EpoR	wt	-	0.080 ± 0.016	-	-		0.089 ± 0.032
EpoR	-	Epo	0.085 ± 0.009	0.069 ± 0.006	0.074 ± 0.011		0.188 ± 0.044
EpoR	wt	Epo	0.073 ± 0.010	0.066 ± 0.013	-		0.135 ± 0.037
EpoR	V617F	-	0.093 ± 0.014	0.072 ± 0.015	-		0.102 ± 0.026
GHR	-	-	0.109 ± 0.016	-	0.093 ± 0.016		0.131 ± 0.041
GHR	wt	-	0.125 ± 0.014	-	-		0.107 ± 0.048
GHR	-	GH	0.106 ± 0.021	0.087 ± 0.022	0.080 ± 0.014		0.127 ± 0.082
GHR	wt	GH	0.097 ± 0.013	0.083 ± 0.017	-		0.089 ± 0.031
GHR	V617F	-	0.104 ± 0.015	0.090 ± 0.018	-		0.084 ± 0.024
GHR	-	GH wt	-	-	-	0.077 ± 0.011	0.117 ± 0.037
GHR	-	GH G146R	-	-	-	0.102 ± 0.010	0.041 ± 0.012

[a] mXFP-tagged receptor, diffusion constant of the total population.

[b] mXFP-tagged receptor, diffusion constant of receptor dimers.

[c] E3-tagged receptor, diffusion constant of the total population.

[d] untagged receptor, diffusion constant of the labeled ligand.

[e] fraction of immobile molecules (for mXFP-tagged receptors or labeled GH, respectively).

Table S2.

PICCS evaluation for control proteins, TpoR, EpoR and GHR.

Condition	**α [%]** [a]	**σ [µm]** [b]
Neg. control	2.6 ± 1.0	0.107 ± 0.048
Pos. control	23.1 ± 2.4	0.057 ± 0.014
TpoR unstim.	2.4 ± 1.7	0.118 ± 0.054
TpoR + TPO	20.8 ± 4.7	0.063 ± 0.008
EpoR unstim.	2.1 ± 1.6	0.097 ± 0.048
EpoR + EPO	15.5 ± 6.9	0.069 ± 0.014
GHR unstim.	2.1 ± 0.8	0.107 ± 0.042
GHR + GH	16.4 ± 2.3	0.057 ± 0.011

[a] The correlated fraction α was related to the localizations of DY647.

[b] The correlation length σ describes the apparent average distance between the co-related molecules, which in the case of molecular interaction is limited by the co-localization precision.

Table S3.

Two-dimensional equilibrium dissociation constants K_D^{2D} for dimerization of different receptors and JAK2.

Receptor	**JAK2**	**ligand**	$\boldsymbol{K_D^{2D}}$ **[µm^{-2}]** [a]	$\boldsymbol{K_D^{2D}}$ **[µm^{-2}]** [b]
TpoR wt	-	Tpo wt	1.4 ± 0.5	
TpoR wt	wt	Tpo wt	0.31 ± 0.07	
TpoR wt	wt	-		112 ± 64
TpoR-ΔECD	wt	-		78 ± 50
TpoR wt	V617F	-	4.6 ± 2.4	5.1 ± 2.6
TpoR-ΔECD	V617F	-		8.4 ±5.2
TpoR wt	V617F	Tpo wt	0.005 ± 0.01	
TpoR W515L	-	-	126 ± 97	
TpoR W515L	wt	-	33 ± 19	
TpoR W515L	V617F	-	3.8 ± 2.2	
EpoR wt	-	Epo wt	3.5 ± 1.1	
EpoR wt	wt	Epo wt	1.3 ± 0.3	
EpoR wt	V617F	-	23 ± 16	
EpoR-ΔECD	wt	-		119 ± 101
EpoR-ΔECD	V617F	-		23 ± 10
GHR wt	-	GH wt	1.29 ± 0.30	
GHR wt	wt	GH wt	0.39 ± 0.0	
		-		
GHR wt	V617F	-	62± 43	

[a] estimated from single molecule co-tracking analysis

[b] estimated from smFRET

Table S4.

Simulated systems (AA – all atom; CG – coarse grained; II – configuration where two TM helices are aligned in parallel; X – cross-shaped orientation of the TM dimer).

System name (force field)	JAK proteins (mutation, residues) Cytokine receptor (mutation, TM/TM pose, residues)	Number of lipid molecules (POPC/ cholesterol/ PIP2/PS)	Water molecules (Na^+, Cl^-)	No. replicas x duration (ns)
$S1_{AA}$ (CHARMM36)	JAK2/JAK2 (WT, 37-1132) TpoR/TpoR (WT, 486-578)	1100/0/0/0	216325 (599, 597)	5 x 1000
$S2_{AA}$ (CHARMM36)	JAK2/JAK2 (V617F, 37-1132) TpoR/TpoR (WT, 486-578)	1100/0/0/0	228177 (634, 632)	5 x 1000
$S3_{AA}$ (CHARMM36)	JAK2/JAK2 (WT, 37-1132) TpoR/TpoR (WT, 486-578)	385/165/0/0 (EC leaflet) 359/165/27/0 (IC leaflet)	235959 (765, 655)	1 x 1000
$S4_{AA}$ (CHARMM36)	JAK2/JAK2 (WT, 37-1132) EpoR/EpoR (WT, II-shape, 31-335)	1100/0/0/0	377794 (1068, 1050)	2 x 1000
$S5_{AA}$ (CHARMM36)	JAK2/JAK2 (WT, 37-1132) EpoR/EpoR (WT, X-shape, 31-335)	1100/0/0/0	435648 (1230, 1212)	2 x 700
$S6_{AA}$ (CHARMM36)	JAK2 PK/PK (WT, 526-810)	N/A	74407 (213,211)	10 x 1000
$S7_{AA}$ (CHARMM36)	JAK2 PK/PK (V617F, 526-810)	N/A	74444 (213,211)	10 x 1000
$S8_{AA}$ (CHARMM36)	TpoR (WT, 486-519)	128/0/0/0	8315 (25, 25)	10 x 1000
$S9_{AA}$ (CHARMM36)	TpoR (W515L, 486-519)	128/0/0/0	8315 (25, 25)	10 x 1000
$S10_{CG}$ (MARTINI)	TpoR/TpoR (WT, 486-519)	264/0/0/0	5284 (58, 58)	10 x 20000
$S11_{CG}$ (MARTINI)	TpoR/TpoR (W515L, 486-519)	264/0/0/0	5284 (58, 58)	10 x 20000
$S12_{CG}$ (MARTINI)	TpoR/TpoR (WT, X, 486-519)	264/0/0/0	5284 (58, 58)	10 x 20000
$S13_{CG}$ (MARTINI)	TpoR/TpoR (W515L, II, 486-519)	264/0/0/0	5284 (58, 58)	10 x 20000
$S14_{CG}$ (MARTINI)	JAK2 (WT, 37-514) TpoR(WT, 486-578)	357/0/0/0 (EC leaflet) 321/0/0/35 (IC leaflet)	24229 (306, 276)	10 x 20000
$S15_{CG}$ (MARTINI)	JAK2 (L224A, 37-514) TpoR(WT, 486-578)	357/0/0/0 (EC leaflet) 321/0/0/35 (IC leaflet)	24223 (306, 276)	10 x 20000
$S16_{CG}$ (MARTINI)	JAK2 (L224E, 37-514) TpoR(WT, 486-578)	357/0/0/0 (EC leaflet) 321/0/0/35 (IC leaflet)	24231 (307, 276)	10 x 20000

Table S5.

Persistent residue-by-residue contacts (>60%) at the PK/PK interface of a JAK2 dimer. The data were calculated from the simulations of system *S6$_{AA}$* using the GROMACS tool *gmx mindist* with a cutoff of 0.6 nm. If two residues were closer to each other than the cutoff distance, they were regarded as a contact pair. This procedure was done for every simulation frame, thus the results indicate the percentage of frames where a contact was observed for a given residue pair. Only interactions with an average contact percentage greater than 60 % are shown.

JAK2 monomer 1 residue	**JAK2 monomer 2 residue**	**Contact percentage**	**JAK2 monomer 1 residue**	**JAK2 monomer 2 residue**	**Contact percentage**
R528	H531	76.63	E596	T530	95.35
R528	E596	60.40	E596	M532	84.95
P529	E596	70.99	E596	H531	76.24
T530	E596	72.38	E596	N533	74.55
H531	E596	66.83	T668	P529	74.95
M532	E596	69.50	L669	P529	70.00
M532	M532	64.65	I670	P529	80.59
M532	E592	63.27	I670	T530	72.08
M532	S593	62.08	S703	N533	60.69
R588	E592	68.12	T705	N533	69.11
R588	F595	62.38	V706	N533	74.06
R588	M532	61.19	V706	V536	61.98
N589	V536	65.05	K728	F537	74.55
N589	N533	64.75	N729	R528	62.67
N589	K539	63.17	N729	Q534	61.09
E592	M532	89.21	L730	R528	71.29
E592	N533	77.23	L730	Q534	68.12
E592	E592	68.51	L730	P529	66.24
E592	V536	60.40	L730	T530	63.86
S593	M532	74.16	N731	R528	66.83
S593	N533	66.34	L732	R528	60.30
F595	E592	61.88			

Table S6.

Most prominent changes in residue contact pairs between the WT and V617F JAK2 PK domains. Contact percentages were initially calculated using the GROMACS tool *gmx mindist* using a cutoff of 0.6 nm. If two residues were closer to each other than the cutoff distance, they were regarded as a contact pair. The procedure was done for every simulation frame, thus the data give the percentage of frames in which a contact was observed for a given residue pair. The results shown are calculated from systems $S6_{AA}$ and $S7_{AA}$ (see Table S4) by subtracting the V617F contact percentage from the WT value. The left side of the table shows contact pairs that are more persistent in the WT case, while the right side lists pairs that are more persistent in the mutant case. Only values above 25 % are shown.

Contact pairs amplified in WT			**Contact pairs amplified in the V617F mutant**		
PK 1 residue	**PK 2 residue**	**Δ(contact percent)**	**PK 1 residue**	**PK 2 residue**	**Δ(contact percent)**
R588	M532	25.54	Q527	Q527	25.25
R588	V536	26.24	P529	M600	26.93
R588	K539	29.80	P529	T668	30.10
N589	N533	25.15	T530	M600	25.35
N589	K539	33.47	M532	E592	27.92
E592	N533	25.45	M532	F595	25.35
F594	N533	28.12	N533	E592	25.74
E596	Q534	28.91	N533	F594	41.49
A597	N533	27.72	N533	F595	30.30
T668	P529	27.62	N533	A597	29.41
I702	N533	25.64	N533	M600	25.15
G701	N533	27.72	Q534	I670	33.47
K728	K603	25.74	Q534	L730	30.30
L730	Q534	33.37	M535	T705	25.64
N731	Q534	35.05	F537	V706	25.15
			V617	R588	30.69
			V617	N589	28.61

Movie S1.

Raw data from dual-color TIRF imaging of HeLa cells expressing mXFP-TpoR post-translationally labeled with ^{Rho11}NB (top) and ^{DY647}NB (bottom). Acquisition frame rate: 30 Hz, Playback: real time.

Movie S2.

Single-step photobleaching of dye-conjugated nanobodies bound to cell surface receptors of live cells. Left: unprocessed TIRFM raw data of ^{Rho11}NB bound to unstimulated mXFP-TpoR and imaged at elevated laser power. Right: superimposition of the fluorescence intensity is shown as a 3D kymograph (ImageJ volume rendering). Acquisition frame rate: 30 Hz, Playback: real time.

Movie S3.

Single-molecule co-tracking as a readout for dimerization of cell surface receptors. A positive control protein mEGFP-MBP-TMD was labeled with ^{Rho11}NB (left, top) and ^{DY647}NB (left, bottom) and dimerized with monoclonal anti-MBP antibody. In the overlay of the zoomed section of both spectral channels (^{Rho11}NB: Red, ^{DY647}NB: Blue), yellow lines indicate co-locomotion trajectories (≥ 10 steps). Acquisition frame rate: 30 Hz, Playback: real time.

Movie S4.

Dimerization of TpoR co-expressed with wt JAK2 in the absence (left) and presence of ligand (center, 5nM TPO, 10 min). Right: ligand-independent dimerization of TpoR co-expressed with JAK2 V617F. Identified co-trajectories (≥ 10 steps) are depicted as yellow lines. Red and Blue signals correspond to receptors labeled with ^{Rho11}NB and ^{DY647}NB, respectively. Acquisition frame rate: 30 Hz, Playback: real time.

Movie S5.

Dimerization of EpoR co-expressed with wt JAK2 in the absence (left) and presence of ligand (center, 5 nM EPO, 10 min). Right: ligand-independent dimerization of EpoR co-expressed with JAK2 V617F. Identified co-trajectories (≥ 10 steps) are depicted as yellow lines. Red and Blue signals correspond to receptors labeled with ^{Rho11}NB and ^{DY647}NB, respectively. Acquisition frame rate: 30 Hz, Playback: real time.

Movie S6.

Dimerization of GHR co-expressed with wt JAK2 in the absence (left) and presence of ligand (center, 5 nM GH, 10 min). Right: ligand-independent dimerization of GHR co-expressed with JAK2 V617F.Identified co-trajectories (≥ 10 steps) are depicted as yellow lines. Red and Blue signals correspond to receptors labeled with ^{Rho11}NB and ^{DY647}NB, respectively. Acquisition frame rate: 30 Hz, Playback: real time.

Movie S7.

Single-molecule FRET of mXFP-ΔECD-TpoR dimerized by JAK2 V617F. Unprocessed raw TIRFM data of mXFP-ΔECD-TpoR (co-expressed with JAK2 V617F-mEGFP) after labeling with ^{Rho11}NB and ^{DY647}NB, imaged at elevated laser intensities. After 15 frames (~0.5 s) of acquisition, the 647 nm laser, used to directly excite ^{DY647}NB, was switched off. Acquisition frame rate: 30 Hz, Playback: real time.

Movie S8.

Heterodimerization of EpoR and TpoR by JAK2 V617F. SNAPf-EpoR (labeled with SNAP-Surface 647: Blue) and mXFP-TpoR (labeled with ^{Rho11}NB: Red) were co-expressed with either JAK2 wt ΔTK (left) or JAK2 V617F ΔTK (right). Identified co-trajectories (≥ 10 steps) are depicted as yellow lines. Acquisition frame rate: 30 Hz, Playback: real time.

Movie S9.

Dimerization of TpoR W515L in the absence (left) of JAK2 and in cells co-expressing JAK2-mEGFP wt (center) or V617F (right). Identified co-trajectories (≥ 10 steps) are depicted as yellow lines. Acquisition frame rate: 30 Hz, Playback: real time.

Movie S10.

Ligand-independent dimerization of TpoR in the presence of JAK2 wt (left) or V617F (right) quantified by ALEX smFRET. Trajectories of donor (red) and acceptor (blue) detected upon direct excitation are overlaid with FRET trajectories (white). Acquisition frame rate: 50 Hz, Playback: real time.

Movie S11.

Atomistic MD simulation of the transmembrane and intracellular sections of TpoR in complex with JAK2 ($S1_{AA}$). JAK2 monomers 1 (blue) and 2 (red) are shown in surface representation with domains highlighted by different shadings: light color: FS; medium color: PK; dark color: TK. TpoR monomers 1 (yellow) and 2 (orange) are shown in ribbon representation.

Movie S12.

Atomistic MD simulation of the ligand-induced EpoR dimer in complex with JAK2 ($S4_{AA}$). JAK2 monomers 1 (blue) and 2 (red) are shown in surface representation with domains highlighted by different shadings: dark color: FS; light color: PK; medium color: TK. EpoR monomers 1 (yellow) and 2 (green) and Epo (purple) are shown in ribbon representation.

Movie S13.

Dimerization of TpoR TM helices and amphipathic motifs (486-519) in CG description ($S12_{CG}$).

References

1. M. Atanasova, A. Whitty, Understanding cytokine and growth factor receptor activation mechanisms. *Crit. Rev. Biochem. Mol. Biol.* **47**, 502–530 (2012). doi:10.3109/10409238.2012.729561 Medline

2. B. C. Cunningham, M. Ultsch, A. M. De Vos, M. G. Mulkerrin, K. R. Clauser, J. A. Wells, Dimerization of the extracellular domain of the human growth hormone receptor by a single hormone molecule. *Science* **254**, 821–825 (1991). doi:10.1126/science.1948064 Medline

3. R. M. Stroud, J. A. Wells, Mechanistic diversity of cytokine receptor signaling across cell membranes. *Sci. STKE* **2004**, re7 (2004). Medline

4. M. J. Waters, A. J. Brooks, JAK2 activation by growth hormone and other cytokines. *Biochem. J.* **466**, 1–11 (2015). doi:10.1042/BJ20141293 Medline

5. J. Gent, P. van Kerkhof, M. Roza, G. Bu, G. J. Strous, Ligand-independent growth hormone receptor dimerization occurs in the endoplasmic reticulum and is required for ubiquitin system-dependent endocytosis. *Proc. Natl. Acad. Sci. U.S.A.* **99**, 9858–9863 (2002). doi:10.1073/pnas.152294299 Medline

6. R. J. Brown, J. J. Adams, R. A. Pelekanos, Y. Wan, W. J. McKinstry, K. Palethorpe, R. M. Seeber, T. A. Monks, K. A. Eidne, M. W. Parker, M. J. Waters, Model for growth hormone receptor activation based on subunit rotation within a receptor dimer. *Nat. Struct. Mol. Biol.* **12**, 814–821 (2005). doi:10.1038/nsmb977 Medline

7. A. J. Brooks, W. Dai, M. L. O'Mara, D. Abankwa, Y. Chhabra, R. A. Pelekanos, O. Gardon, K. A. Tunny, K. M. Blucher, C. J. Morton, M. W. Parker, E. Sierecki, Y. Gambin, G. A. Gomez, K. Alexandrov, I. A. Wilson, M. Doxastakis, A. E. Mark, M. J. Waters, Mechanism of activation of protein kinase JAK2 by the growth hormone receptor. *Science* **344**, 1249783 (2014). doi:10.1126/science.1249783 Medline

8. S. Tenhumberg, B. Schuster, L. Zhu, M. Kovaleva, J. Scheller, K.-J. Kallen, S. Rose-John, gp130 dimerization in the absence of ligand: Preformed cytokine receptor complexes. *Biochem. Biophys. Res. Commun.* **346**, 649–657 (2006). doi:10.1016/j.bbrc.2006.05.173 Medline

9. M. Zaks-Zilberman, A. E. Harrington, T. Ishino, I. M. Chaiken, Interleukin-5 receptor subunit oligomerization and rearrangement revealed by fluorescence resonance energy transfer imaging. *J. Biol. Chem.* **283**, 13398–13406 (2008). doi:10.1074/jbc.M710230200 Medline

10. C. D. Krause, N. Lavnikova, J. Xie, E. Mei, O. V. Mirochnitchenko, Y. Jia, R. M. Hochstrasser, S. Pestka, Preassembly and ligand-induced restructuring of the chains of

the IFN-gamma receptor complex: The roles of Jak kinases, Stat1 and the receptor chains. *Cell Res.* **16**, 55–69 (2006). doi:10.1038/sj.cr.7310008 Medline

11. C. D. Krause, E. Mei, J. Xie, Y. Jia, M. A. Bopp, R. M. Hochstrasser, S. Pestka, Seeing the light: Preassembly and ligand-induced changes of the interferon gamma receptor complex in cells. *Mol. Cell. Proteomics* **1**, 805–815 (2002). doi:10.1074/mcp.M200065-MCP200 Medline

12. C. D. Krause, E. Mei, O. Mirochnitchenko, N. Lavnikova, J. Xie, Y. Jia, R. M. Hochstrasser, S. Pestka, Interactions among the components of the interleukin-10 receptor complex. *Biochem. Biophys. Res. Commun.* **340**, 377–385 (2006). doi:10.1016/j.bbrc.2005.11.182 Medline

13. R. L. Levine, M. Wadleigh, J. Cools, B. L. Ebert, G. Wernig, B. J. P. Huntly, T. J. Boggon, I. Wlodarska, J. J. Clark, S. Moore, J. Adelsperger, S. Koo, J. C. Lee, S. Gabriel, T. Mercher, A. D'Andrea, S. Fröhling, K. Döhner, P. Marynen, P. Vandenberghe, R. A. Mesa, A. Tefferi, J. D. Griffin, M. J. Eck, W. R. Sellers, M. Meyerson, T. R. Golub, S. J. Lee, D. G. Gilliland, Activating mutation in the tyrosine kinase JAK2 in polycythemia vera, essential thrombocythemia, and myeloid metaplasia with myelofibrosis. *Cancer Cell* **7**, 387–397 (2005). doi:10.1016/j.ccr.2005.03.023 Medline

14. W. Vainchenker, S. N. Constantinescu, JAK/STAT signaling in hematological malignancies. *Oncogene* **32**, 2601–2613 (2013). doi:10.1038/onc.2012.347 Medline

15. V. C. Broudy, N. Lin, M. Brice, B. Nakamoto, T. Papayannopoulou, Erythropoietin receptor characteristics on primary human erythroid cells. *Blood* **77**, 2583–2590 (1991). doi:10.1182/blood.V77.12.2583.2583 Medline

16. W. J. McKinstry, C.-L. Li, J. E. J. Rasko, N. A. Nicola, G. R. Johnson, D. Metcalf, Cytokine receptor expression on hematopoietic stem and progenitor cells. *Blood* **89**, 65–71 (1997). doi:10.1182/blood.V89.1.65 Medline

17. N. Komatsu, M. Kunitama, M. Yamada, T. Hagiwara, T. Kato, H. Miyazaki, M. Eguchi, M. Yamamoto, Y. Miura, Establishment and characterization of the thrombopoietin-dependent megakaryocytic cell line, UT-7/TPO. *Blood* **87**, 4552–4560 (1996). doi:10.1182/blood.V87.11.4552.bloodjournal87114552 Medline

18. See supplementary materials.

19. I. Moraga, G. Wernig, S. Wilmes, V. Gryshkova, C. P. Richter, W.-J. Hong, R. Sinha, F. Guo, H. Fabionar, T. S. Wehrman, P. Krutzik, S. Demharter, I. Plo, I. L. Weissman, P. Minary, R. Majeti, S. N. Constantinescu, J. Piehler, K. C. Garcia, Tuning cytokine receptor signaling by re-orienting dimer geometry with surrogate ligands. *Cell* **160**, 1196–1208 (2015). doi:10.1016/j.cell.2015.02.011 Medline

20. I. Chung, R. Akita, R. Vandlen, D. Toomre, J. Schlessinger, I. Mellman, Spatial control of EGF receptor activation by reversible dimerization on living cells. *Nature* **464**, 783–787 (2010). doi:10.1038/nature08827 Medline

21. I. S. Hitchcock, M. M. Chen, J. R. King, K. Kaushansky, YRRL motifs in the cytoplasmic domain of the thrombopoietin receptor regulate receptor internalization and degradation. *Blood* **112**, 2222–2231 (2008). doi:10.1182/blood-2008-01-134049 Medline

22. G. B. Bulut, R. Sulahian, H. Yao, L. J. S. Huang, Cbl ubiquitination of p85 is essential for Epo-induced EpoR endocytosis. *Blood* **122**, 3964–3972 (2013). doi:10.1182/blood-2013-05-506212 Medline

23. Y. Yano, A. Yano, S. Oishi, Y. Sugimoto, G. Tsujimoto, N. Fujii, K. Matsuzaki, Coiled-coil tag—Probe system for quick labeling of membrane receptors in living cell. *ACS Chem. Biol.* **3**, 341–345 (2008). doi:10.1021/cb8000556 Medline

24. S. Semrau, L. Holtzer, M. González-Gaitán, T. Schmidt, Quantification of biological interactions with particle image cross-correlation spectroscopy (PICCS). *Biophys. J.* **100**, 1810–1818 (2011). doi:10.1016/j.bpj.2010.12.3746 Medline

25. K. C. Leung, N. Doyle, M. Ballesteros, M. J. Waters, K. K. Ho, Insulin regulation of human hepatic growth hormone receptors: Divergent effects on biosynthesis and surface translocation. *J. Clin. Endocrinol. Metab.* **85**, 4712–4720 (2000). Medline

26. G. Fuh, B. C. Cunningham, R. Fukunaga, S. Nagata, D. V. Goeddel, J. A. Wells, Rational design of potent antagonists to the human growth hormone receptor. *Science* **256**, 1677–1680 (1992). doi:10.1126/science.256.5064.1677 Medline

27. S. Elliott, T. Lorenzini, D. Chang, J. Barzilay, E. Delorme, Mapping of the active site of recombinant human erythropoietin. *Blood* **89**, 493–502 (1997). doi:10.1182/blood.V89.2.493 Medline

28. N. F. Endres, R. Das, A. W. Smith, A. Arkhipov, E. Kovacs, Y. Huang, J. G. Pelton, Y. Shan, D. E. Shaw, D. E. Wemmer, J. T. Groves, J. Kuriyan, Conformational coupling across the plasma membrane in activation of the EGF receptor. *Cell* **152**, 543–556 (2013). doi:10.1016/j.cell.2012.12.032 Medline

29. O. Silvennoinen, S. R. Hubbard, Molecular insights into regulation of JAK2 in myeloproliferative neoplasms. *Blood* **125**, 3388–3392 (2015). doi:10.1182/blood-2015-01-621110 Medline

30. X. Lu, R. Levine, W. Tong, G. Wernig, Y. Pikman, S. Zarnegar, D. G. Gilliland, H. Lodish, Expression of a homodimeric type I cytokine receptor is required for JAK2V617F-mediated transformation. *Proc. Natl. Acad. Sci. U.S.A.* **102**, 18962–18967 (2005). doi:10.1073/pnas.0509714102 Medline

31. X. Lu, L. J. Huang, H. F. Lodish, Dimerization by a cytokine receptor is necessary for constitutive activation of JAK2V617F. *J. Biol. Chem.* **283**, 5258–5266 (2008). doi:10.1074/jbc.M707125200 Medline

32. A. Dusa, C. Mouton, C. Pecquet, M. Herman, S. N. Constantinescu, JAK2 V617F constitutive activation requires JH2 residue F595: A pseudokinase domain target for specific inhibitors. *PLOS ONE* **5**, e11157 (2010). doi:10.1371/journal.pone.0011157 Medline

33. J. Staerk, C. Lacout, T. Sato, S. O. Smith, W. Vainchenker, S. N. Constantinescu, An amphipathic motif at the transmembrane-cytoplasmic junction prevents autonomous activation of the thrombopoietin receptor. *Blood* **107**, 1864–1871 (2006). doi:10.1182/blood-2005-06-2600 Medline

34. Y. Pikman, B. H. Lee, T. Mercher, E. McDowell, B. L. Ebert, M. Gozo, A. Cuker, G. Wernig, S. Moore, I. Galinsky, D. J. DeAngelo, J. J. Clark, S. J. Lee, T. R. Golub, M. Wadleigh, D. G. Gilliland, R. L. Levine, MPLW515L is a novel somatic activating mutation in myelofibrosis with myeloid metaplasia. *PLOS Med.* **3**, e270 (2006). doi:10.1371/journal.pmed.0030270 Medline

35. J. P. Defour, M. Itaya, V. Gryshkova, I. C. Brett, C. Pecquet, T. Sato, S. O. Smith, S. N. Constantinescu, Tryptophan at the transmembrane-cytosolic junction modulates thrombopoietin receptor dimerization and activation. *Proc. Natl. Acad. Sci. U.S.A.* **110**, 2540–2545 (2013). doi:10.1073/pnas.1211560110 Medline

36. S. N. Constantinescu, T. Keren, M. Socolovsky, H. Nam, Y. I. Henis, H. F. Lodish, Ligand-independent oligomerization of cell-surface erythropoietin receptor is mediated by the transmembrane domain. *Proc. Natl. Acad. Sci. U.S.A.* **98**, 4379–4384 (2001). doi:10.1073/pnas.081069198 Medline

37. Y. Royer, J. Staerk, M. Costuleanu, P. J. Courtoy, S. N. Constantinescu, Janus kinases affect thrombopoietin receptor cell surface localization and stability. *J. Biol. Chem.* **280**, 27251–27261 (2005). doi:10.1074/jbc.M501376200 Medline

38. C. Pecquet, J. Staerk, R. Chaligné, V. Goss, K. A. Lee, X. Zhang, J. Rush, J. Van Hees, H. A. Poirel, J.-M. Scheiff, W. Vainchenker, S. Giraudier, R. D. Polakiewicz, S. N. Constantinescu, Induction of myeloproliferative disorder and myelofibrosis by thrombopoietin receptor W515 mutants is mediated by cytosolic tyrosine 112 of the receptor. *Blood* **115**, 1037–1048 (2010). doi:10.1182/blood-2008-10-183558 Medline

39. K. Mohan, G. Ueda, A. R. Kim, K. M. Jude, J. A. Fallas, Y. Guo, M. Hafer, Y. Miao, R. A. Saxton, J. Piehler, V. G. Sankaran, D. Baker, K. C. Garcia, Topological control of cytokine receptor signaling induces differential effects in hematopoiesis. *Science* **364**, eaav7532 (2019). doi:10.1126/science.aav7532 Medline

40. H. M. Hammarén, A. T. Virtanen, J. Raivola, O. Silvennoinen, The regulation of JAKs in cytokine signaling and its breakdown in disease. *Cytokine* **118**, 48–63 (2019). doi:10.1016/j.cyto.2018.03.041 Medline

41. Y. Shan, K. Gnanasambandan, D. Ungureanu, E. T. Kim, H. Hammarén, K. Yamashita, O. Silvennoinen, D. E. Shaw, S. R. Hubbard, Molecular basis for pseudokinase-dependent autoinhibition of JAK2 tyrosine kinase. *Nat. Struct. Mol. Biol.* **21**, 579–584 (2014). doi:10.1038/nsmb.2849 Medline

42. P. J. Lupardus, M. Ultsch, H. Wallweber, P. Bir Kohli, A. R. Johnson, C. Eigenbrot, Structure of the pseudokinase-kinase domains from protein kinase TYK2 reveals a mechanism for Janus kinase (JAK) autoinhibition. *Proc. Natl. Acad. Sci. U.S.A.* **111**, 8025–8030 (2014). doi:10.1073/pnas.1401180111 Medline

43. S. R. Hubbard, Mechanistic Insights into Regulation of JAK2 Tyrosine Kinase. *Front. Endocrinol.* **8**, 361 (2018). doi:10.3389/fendo.2017.00361 Medline

44. H. M. Hammarén, A. T. Virtanen, B. G. Abraham, H. Peussa, S. R. Hubbard, O. Silvennoinen, Janus kinase 2 activation mechanisms revealed by analysis of suppressing mutations. *J. Allergy Clin. Immunol.* **143**, 1549–1559.e6 (2019). Medline

45. A. V. Toms, A. Deshpande, R. McNally, Y. Jeong, J. M. Rogers, C. U. Kim, S. M. Gruner, S. B. Ficarro, J. A. Marto, M. Sattler, J. D. Griffin, M. J. Eck, Structure of a pseudokinase-domain switch that controls oncogenic activation of Jak kinases. *Nat. Struct. Mol. Biol.* **20**, 1221–1223 (2013). doi:10.1038/nsmb.2673 Medline

46. R. M. Bandaranayake, D. Ungureanu, Y. Shan, D. E. Shaw, O. Silvennoinen, S. R. Hubbard, Crystal structures of the JAK2 pseudokinase domain and the pathogenic mutant V617F. *Nat. Struct. Mol. Biol.* **19**, 754–759 (2012). doi:10.1038/nsmb.2348 Medline

47. R. D. Ferrao, H. J. Wallweber, P. J. Lupardus, Receptor-mediated dimerization of JAK2 FERM domains is required for JAK2 activation. *eLife* **7**, e38089 (2018). doi:10.7554/eLife.38089 Medline

48. K. Gnanasambandan, A. Magis, P. P. Sayeski, The constitutive activation of Jak2-V617F is mediated by a π stacking mechanism involving phenylalanines 595 and 617. *Biochemistry* **49**, 9972–9984 (2010). doi:10.1021/bi1014858 Medline

49. L. Zhao, H. Dong, C. C. Zhang, L. Kinch, M. Osawa, M. Iacovino, N. V. Grishin, M. Kyba, L. J. Huang, A JAK2 interdomain linker relays Epo receptor engagement signals to kinase activation. *J. Biol. Chem.* **284**, 26988–26998 (2009). doi:10.1074/jbc.M109.011387 Medline

50. R. Kumari, R. Kumar, Open Source Drug Discovery Consortium, A. Lynn, g_mmpbsa—A GROMACS tool for high-throughput MM-PBSA calculations. *J. Chem. Inf. Model.* **54**, 1951–1962 (2014). doi:10.1021/ci500020m Medline

51. I. Remy, I. A. Wilson, S. W. Michnick, Erythropoietin receptor activation by a ligand-induced conformation change. *Science* **283**, 990–993 (1999). doi:10.1126/science.283.5404.990 Medline

52. E. E. Matthews, D. Thévenin, J. M. Rogers, L. Gotow, P. D. Lira, L. A. Reiter, W. H. Brissette, D. M. Engelman, Thrombopoietin receptor activation: Transmembrane helix dimerization, rotation, and allosteric modulation. *FASEB J.* **25**, 2234–2244 (2011). doi:10.1096/fj.10-178673 Medline

53. J. Schindelin, I. Arganda-Carreras, E. Frise, V. Kaynig, M. Longair, T. Pietzsch, S. Preibisch, C. Rueden, S. Saalfeld, B. Schmid, J.-Y. Tinevez, D. J. White, V. Hartenstein, K. Eliceiri, P. Tomancak, A. Cardona, Fiji: An open-source platform for biological-image analysis. *Nat. Methods* **9**, 676–682 (2012). doi:10.1038/nmeth.2019 Medline

54. A. Kirchhofer, J. Helma, K. Schmidthals, C. Frauer, S. Cui, A. Karcher, M. Pellis, S. Muyldermans, C. S. Casas-Delucchi, M. C. Cardoso, H. Leonhardt, K.-P. Hopfner, U. Rothbauer, Modulation of protein properties in living cells using nanobodies. *Nat. Struct. Mol. Biol.* **17**, 133–138 (2010). doi:10.1038/nsmb.1727 Medline

55. S. Waichman, M. Bhagawati, Y. Podoplelova, A. Reichel, A. Brunk, D. Paterok, J. Piehler, Functional immobilization and patterning of proteins by an enzymatic transfer reaction. *Anal. Chem.* **82**, 1478–1485 (2010). doi:10.1021/ac902608a Medline

56. F. L. Graham, A. J. van der Eb, A new technique for the assay of infectivity of human adenovirus 5 DNA. *Virology* **52**, 456–467 (1973). doi:10.1016/0042-6822(73)90341-3 Medline

57. C. You, C. P. Richter, S. Löchte, S. Wilmes, J. Piehler, Dynamic submicroscopic signaling zones revealed by pair correlation tracking and localization microscopy. *Anal. Chem.* **86**, 8593–8602 (2014). doi:10.1021/ac501127r Medline

58. S. Wilmes, O. Beutel, Z. Li, V. Francois-Newton, C. P. Richter, D. Janning, C. Kroll, P. Hanhart, K. Hötte, C. You, G. Uzé, S. Pellegrini, J. Piehler, Receptor dimerization dynamics as a regulatory valve for plasticity of type I interferon signaling. *J. Cell Biol.* **209**, 579–593 (2015). doi:10.1083/jcb.201412049 Medline

59. J. Vogelsang, R. Kasper, C. Steinhauer, B. Person, M. Heilemann, M. Sauer, P. Tinnefeld, A reducing and oxidizing system minimizes photobleaching and blinking of fluorescent dyes. *Angew. Chem. Int. Ed.* **47**, 5465–5469 (2008). doi:10.1002/anie.200801518 Medline

60. A. Sergé, N. Bertaux, H. Rigneault, D. Marguet, Dynamic multiple-target tracing to probe spatiotemporal cartography of cell membranes. *Nat. Methods* **5**, 687–694 (2008). doi:10.1038/nmeth.1233 Medline

61. K. Jaqaman, D. Loerke, M. Mettlen, H. Kuwata, S. Grinstein, S. L. Schmid, G. Danuser, Robust single-particle tracking in live-cell time-lapse sequences. *Nat. Methods* **5**, 695–702 (2008). doi:10.1038/nmeth.1237 Medline

62. F. Roder, S. Wilmes, C. P. Richter, J. Piehler, Rapid transfer of transmembrane proteins for single molecule dimerization assays in polymer-supported membranes. *ACS Chem. Biol.* **9**, 2479–2484 (2014). doi:10.1021/cb5005806 Medline

63. S. Semrau, T. Schmidt, Particle image correlation spectroscopy (PICS): Retrieving nanometer-scale correlations from high-density single-molecule position data. *Biophys. J.* **92**, 613–621 (2007). doi:10.1529/biophysj.106.092577 Medline

64. T. Wedeking, S. Löchte, O. Birkholz, A. Wallenstein, J. Trahe, J. Klingauf, J. Piehler, C. You, Spatiotemporally Controlled Reorganization of Signaling Complexes in the Plasma Membrane of Living Cells. *Small* **11**, 5912–5918 (2015). doi:10.1002/smll.201502132 Medline

65. T. Wedeking, S. Löchte, C. P. Richter, M. Bhagawati, J. Piehler, C. You, Single Cell GFP-Trap Reveals Stoichiometry and Dynamics of Cytosolic Protein Complexes. *Nano Lett.* **15**, 3610–3615 (2015). doi:10.1021/acs.nanolett.5b01153 Medline

66. S. Löchte, S. Waichman, O. Beutel, C. You, J. Piehler, Live cell micropatterning reveals the dynamics of signaling complexes at the plasma membrane. *J. Cell Biol.* **207**, 407–418 (2014). doi:10.1083/jcb.201406032 Medline

67. R. McNally, A. V. Toms, M. J. Eck, Crystal Structure of the FERM-SH2 Module of Human Jak2. *PLOS ONE* **11**, e0156218 (2016). doi:10.1371/journal.pone.0156218 Medline

68. P. J. Lupardus, G. Skiniotis, A. J. Rice, C. Thomas, S. Fischer, T. Walz, K. C. Garcia, Structural snapshots of full-length Jak1, a transmembrane gp130/IL-6/IL-6Rα cytokine receptor complex, and the receptor-Jak1 holocomplex. *Structure* **19**, 45–55 (2011). doi:10.1016/j.str.2010.10.010 Medline

69. E. L. Wu, X. Cheng, S. Jo, H. Rui, K. C. Song, E. M. Dávila-Contreras, Y. Qi, J. Lee, V. Monje-Galvan, R. M. Venable, J. B. Klauda, W. Im, CHARMM-GUI Membrane Builder toward realistic biological membrane simulations. *J. Comput. Chem.* **35**, 1997–2004 (2014). doi:10.1002/jcc.23702 Medline

70. A. Šali, T. L. Blundell, Comparative protein modelling by satisfaction of spatial restraints. *J. Mol. Biol.* **234**, 779–815 (1993). doi:10.1006/jmbi.1993.1626 Medline

71. I. Massova, P. A. Kollman, Combined molecular mechanical and continuum solvent approach (MM-PBSA/GBSA) to predict ligand binding. *Perspect. Drug Discov. Des.* **18**, 113–135 (2000). doi:10.1023/A:1008763014207

72. Q. Li, Y. L. Wong, Q. Huang, C. Kang, Structural insight into the transmembrane domain and the juxtamembrane region of the erythropoietin receptor in micelles. *Biophys. J.* **107**, 2325–2336 (2014). doi:10.1016/j.bpj.2014.10.013 Medline

73. S. Jo, T. Kim, V. G. Iyer, W. Im, CHARMM-GUI: A web-based graphical user interface for CHARMM. *J. Comput. Chem.* **29**, 1859–1865 (2008). doi:10.1002/jcc.20945 Medline

74. R. Ferrao, H. J. A. Wallweber, H. Ho, C. Tam, Y. Franke, J. Quinn, P. J. Lupardus, The Structural Basis for Class II Cytokine Receptor Recognition by JAK1. *Structure* **24**, 897–905 (2016). doi:10.1016/j.str.2016.03.023 Medline

75. H. J. Wallweber, C. Tam, Y. Franke, M. A. Starovasnik, P. J. Lupardus, Structural basis of recognition of interferon-α receptor by tyrosine kinase 2. *Nat. Struct. Mol. Biol.* **21**, 443–448 (2014). doi:10.1038/nsmb.2807 Medline

76. D. H. de Jong, G. Singh, W. F. D. Bennett, C. Arnarez, T. A. Wassenaar, L. V. Schäfer, X. Periole, D. P. Tieleman, S. J. Marrink, Improved Parameters for the Martini Coarse-Grained Protein Force Field. *J. Chem. Theory Comput.* **9**, 687–697 (2013). doi:10.1021/ct300646g Medline

77. J. Lee, X. Cheng, J. M. Swails, M. S. Yeom, P. K. Eastman, J. A. Lemkul, S. Wei, J. Buckner, J. C. Jeong, Y. Qi, S. Jo, V. S. Pande, D. A. Case, C. L. Brooks 3rd, A. D. MacKerell Jr., J. B. Klauda, W. Im, CHARMM-GUI Input Generator for NAMD, GROMACS, AMBER, OpenMM, and CHARMM/OpenMM Simulations Using the CHARMM36 Additive Force Field. *J. Chem. Theory Comput.* **12**, 405–413 (2016). doi:10.1021/acs.jctc.5b00935 Medline

78. J. Huang, A. D. MacKerell Jr., CHARMM36 all-atom additive protein force field: Validation based on comparison to NMR data. *J. Comput. Chem.* **34**, 2135–2145 (2013). doi:10.1002/jcc.23354 Medline

79. S. Lee, A. Tran, M. Allsopp, J. B. Lim, J. Hénin, J. B. Klauda, CHARMM36 united atom chain model for lipids and surfactants. *J. Phys. Chem. B* **118**, 547–556 (2014). doi:10.1021/jp410344g Medline

80. W. L. Jorgensen, J. Chandrasekhar, J. D. Madura, R. W. Impey, M. L. Klein, Comparison of simple potential functions for simulating liquid water. *J. Chem. Phys.* **79**, 926–935 (1983). doi:10.1063/1.445869

81. S. Y. Noskov, B. Roux, Control of ion selectivity in LeuT: Two Na^+ binding sites with two different mechanisms. *J. Mol. Biol.* **377**, 804–818 (2008). doi:10.1016/j.jmb.2008.01.015 Medline

82. M. J. Abraham, T. Murtola, R. Schulz, S. Páll, J. C. Smith, B. Hess, E. Lindahl, GROMACS: High performance molecular simulations through multi-level parallelism from laptops to supercomputers. *SoftwareX* **1–2**, 19–25 (2015). doi:10.1016/j.softx.2015.06.001

83. S. Páll, B. Hess, A flexible algorithm for calculating pair interactions on SIMD architectures. *Comput. Phys. Commun.* **184**, 2641–2650 (2013). doi:10.1016/j.cpc.2013.06.003

84. B. Hess, H. Bekker, H. J. C. Berendsen, J. G. E. M. Fraaije, LINCS: A linear constraint solver for molecular simulations. *J. Comput. Chem.* **18**, 1463–1472 (1997). doi:10.1002/(SICI)1096-987X(199709)18:12<1463:AID-JCC4>3.0.CO;2-H

85. T. Darden, D. York, L. Pedersen, Particle Mesh Ewald - an N.Log(N) Method for Ewald Sums in Large Systems. *J. Chem. Phys.* **98**, 10089–10092 (1993). doi:10.1063/1.464397

86. W. G. Hoover, Canonical dynamics: Equilibrium phase-space distributions. *Phys. Rev. A* **31**, 1695–1697 (1985). doi:10.1103/PhysRevA.31.1695 Medline

87. S. Nosé, A Unified Formulation of the Constant Temperature Molecular-Dynamics Methods. *J. Chem. Phys.* **81**, 511–519 (1984). doi:10.1063/1.447334

88. M. Parrinello, A. Rahman, Polymorphic transitions in single crystals: A new molecular dynamics method. *J. Appl. Phys.* **52**, 7182–7190 (1981). doi:10.1063/1.328693

89. D. H. de Jong, S. Baoukina, H. I. Ingólfsson, S. J. Marrink, Martini straight: Boosting performance using a shorter cutoff and GPUs. *Comput. Phys. Commun.* **199**, 1–7 (2016). doi:10.1016/j.cpc.2015.09.014